
Patterns of lithology, structure, alteration and trace elements around high-grade ore zones at the Turquoise Ridge gold deposit, Getchell District, Nevada

Michael Cassinerio and John Muntean*

ABSTRACT

Few data sets have been published that depict the extent of hydrothermal features surrounding high-grade ore bodies in Carlin-type gold deposits (CTGDs), making exploration, development, and production difficult, especially where visually unaltered, unmineralized rocks occur in close proximity to ore. Patterns of lithology, structure, visible hydrothermal alteration, trace elements, and clay mineralogy are presented to test for the presence of haloes that can potentially be used as vectoring tools in honing in on high-grade ore zones at the Turquoise Ridge CTGD. Closely-spaced diamond drill holes along a cross-section across the High Grade Bullion (HGB) ore zone at the north end of Turquoise Ridge were logged in detail. The logging information, gold assays, multi-element analyses, and spectral reflectance analyses were plotted on a 1:600 scale cross-section, from which controls on gold (Au) grade and haloes to ore zones were interpreted.

The Eocene-age Turquoise Ridge CTGD is hosted within a complexly deformed package of Cambrian-Ordovician sedimentary and volcanic rocks that is characterized by rapid facies changes and soft-sediment deformation. The lowermost unit comprises variably calcareous, carbonaceous mudstones and limestones that are overlain by a series of sedimentary debris flow breccias. Above the breccias are deformed tuffaceous mudstones and limestones, which inter-finger to the northeast with a thick sequence of pillow basalt. Both the sedimentary debris flow breccias and the basalt pinch out to the south, and are interpreted to be controlled by a Cambrian-Ordovician, west-northwest trending, northeast-facing basin margin. Further up section the rocks are mainly mudstone, basalt, and chert. The rocks are intruded by Cretaceous dacite porphyry dikes. The Turquoise Ridge deposit occurs in the hanging wall of the east-dipping, north-northwest-striking Getchell fault zone, which is the main fault in the district.

Much of the HGB ore zone occurs along complex intersections between steep, small-displacement faults, folds, and fractured calcareous lithologies, especially within the series of sedimentary breccias. The Au grades commonly show abrupt variations, locally changing from ≥ 17 ppm to < 0.34 ppm within a few meters. Zones of ≥ 0.34 ppm Au extend up to 120 meters above and up to 150 meters below the HGB; occur within the Getchell fault; and occur along several steep, small-displacement, antithetic faults in the hanging wall of the Getchell fault. Visible alteration, consisting of decalcification, argillization, and silicification, strongly correlates with Au grades of ≥ 0.34 ppm.

Correlation matrices and factor analysis of downhole multi-element data show Au is strongly associated with Hg, As, W, S, Tl, Sb, and Te, and has a strong negative correlation with Ca, Mg, and Sr that is consistent with decalcification being the main alteration type. Values of ≥ 100 ppm As form a halo up to 30 m beyond the 0.34 ppm Au contour and visible alteration, whereas the 5 ppm Sb contour forms a halo up to 12 m wide. With the possible exception of Hg, other features derived from the multi-ele-

*E-mail: munteanj@unr.edu

ment data, including Tl, Te, degree of sulfidation (DOS), Au factor scores (derived from factor analysis), and Ca (to monitor decalcification) do not form significant, coherent haloes to the 0.34 ppm Au contour or visible alteration.

Kaolinite and illite commonly occur in zones of ≥ 0.34 ppm Au. Inspection of samples from ore zones using an SEM show they are intimately intergrown with arsenian pyrite. Kaolinite- and illite-bearing fractures surfaces form incoherent haloes extending up to 20 m beyond visible alteration in otherwise unaltered rocks. Limited analyses of these fractures using a Niton handheld XRF show the fractures can contain significantly higher As than the adjacent wall rock.

The lack of wide, coherent haloes of various hydrothermal features surrounding ore at Turquoise Ridge is suggestive of a restrictive, fracture-controlled fluid flow network, rather than large-scale, pervasive, lithologically-controlled fluid flow. Ore fluids likely ascended along the pre-existing Getchell fault zone and into the steep, small-displacement, antithetic faults in the hanging wall and the main dacite porphyry dike before encountering highly fractured, reactive carbonate-bearing lithologies, especially the sedimentary breccias and deformed mudstones and limestones adjacent to the basalt. Increased surface area in these zones allowed more fluid:rock interaction, which resulted in more pervasive carbonate dissolution, sulfidation, and Au deposition in the HGB. A large zone $< 25\%$ RQD values that surrounds ore supports exploitation of these pre-existing fracture networks and as well as fracturing caused by collapse during carbonate dissolution associated with ore formation.

Key Words: Turquoise Ridge, Getchell, Osgood Mountains, Carlin-type, gold, High Grade Bullion zone, hydrothermal alteration, trace elements, clay mineralogy

INTRODUCTION

Carlin-type gold deposits (CTGDs) in Nevada represent one of the largest concentrations of gold (Au) deposits in the world (Fig. 1). Nearly 200 Moz of Au in CTGDs have either been produced or occur as remaining reserves and resources. Current production accounts for 60% of annual U.S. Au production and 6.5% of annual global production, making the U.S. the 4th largest Au-producing nation in the world (NBMG, 2009). CTGDs are epigenetic, disseminated auriferous pyrite deposits characterized by carbonate dissolution, argillic alteration, and silicification of typically Paleozoic calcareous sedimentary rocks (Hofstra and Cline, 2000; Cline et al., 2005). Au occurs as solid solution in pyrite and less commonly as submicron native Au particles in pyrite (Well and Mullens, 1973; Arehart et al., 1993a; Simon et al., 1999; Reich et al., 2005). Late ore-stage minerals commonly include orpiment, realgar, stibnite, and barite (Hofstra and Cline, 2000; Cline et al., 2005). CTGDs commonly occur in clusters along linear “trends” and formed mainly during the late Eocene (Hofstra et al., 1999; Arehart et al., 2003; Cline et al., 2005).

District-scale exploration for CTGDs has traditionally targeted zones of anomalous gold assays and elevated associated trace elements, namely arsenic, mercury, antimony and thallium, as well as favorable alteration, especially jasperoids because of their resistant nature. In addition, exploration has targeted structural culminations and intersections between

calcareous stratigraphic horizons and high-angle structures. Future discoveries will undoubtedly focus on covered, deep ore bodies, requiring costly drilling. Continued research documenting not only mappable macroscopic features, but also cryptic features, proximal and distal to known ore bodies could very well provide tools to assist in zeroing in on an unexposed ore body and mitigate exploration costs by gaining more vectoring information from each drill hole.

Understanding of the vertical and lateral extent of Carlin-type hydrothermal systems has lagged behind porphyry and epithermal deposits (cf. Lowell and Guilbert, 1970; Gustafson and Hunt, 1975; Seedorff et al., 2005; Buchanan, 1981; Hedenquist et al., 2000; Simmons, et al., 2005). Published studies that mapped the relationship between gold grade and lithology, structure, alteration and trace elements at the scale of individual CTGDs include those at the Carlin (Bakken and Einaudi, 1986; Kuehn and Rose, 1992), Deep Star (Heitt et al., 2003), Gold Quarry (Harlan et al., 2002), Alligator Ridge (Ilchik, 1990) and Twin Creeks deposits (Stenger et al., 1998). Increasingly, exploration for CTGDs is being focused on underground targets that require high grades to be mined. Grades in known underground deposits can vary from > 5 – 20 g/t Au in the ore to < 0.5 g/t within a few meters peripherally (e.g., Deep Star, Heit et al., 2003), making exploration, development and mining very difficult. Few maps or cross-sections have been published showing patterns of hydrothermal features around individual high-grade ore zones.

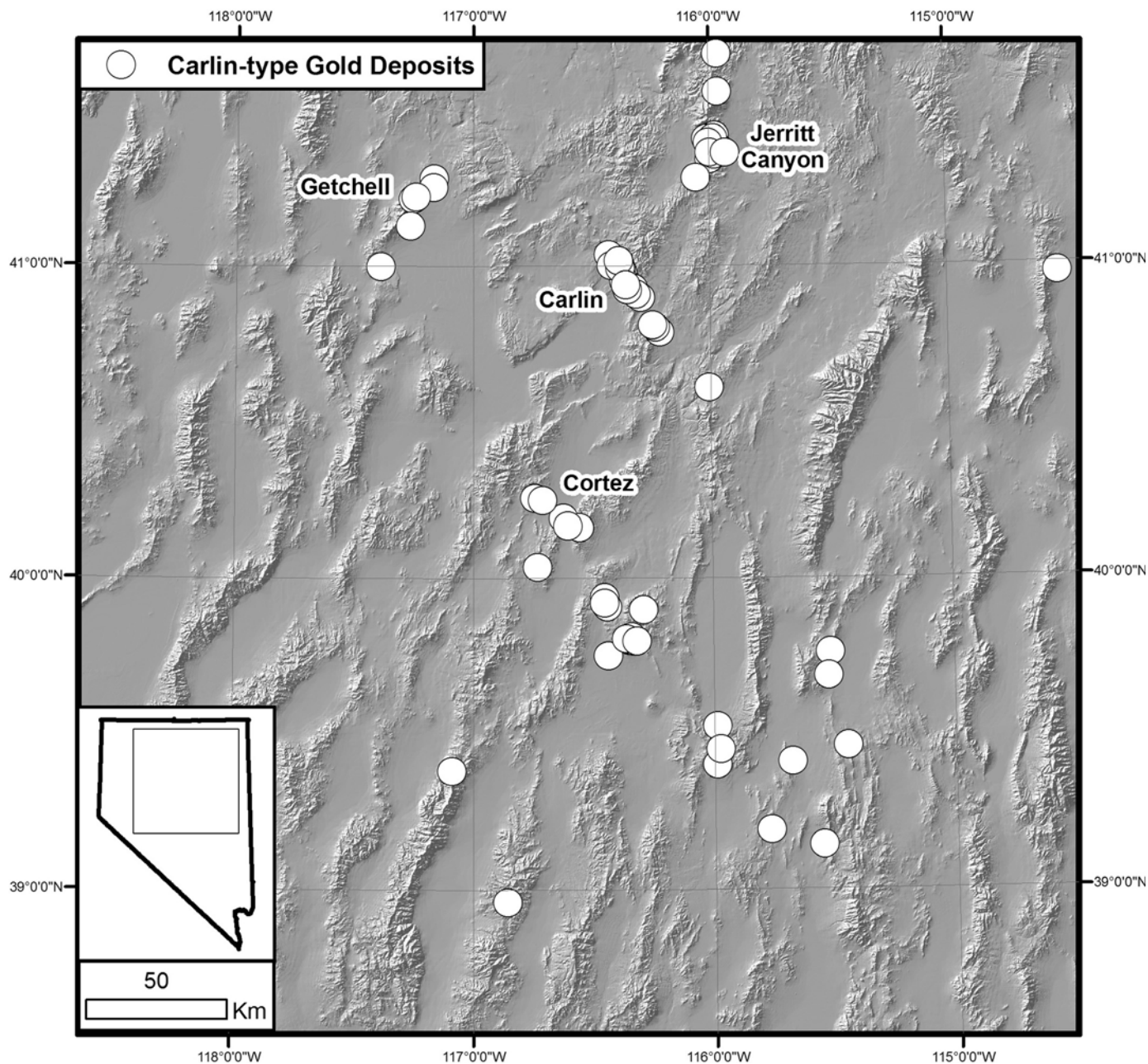


Figure 1. Digital elevation model of northern Nevada, showing locations of CTGDs and the locations of the four large clusters of large CTGDs, including Getchell.

This paper presents patterns of lithology, structure, hydrothermal alteration, Au grade, trace element concentrations, degree of sulfidation, and clay minerals around the High Grade Bullion (HGB) ore zone along a cross-section through the underground Turquoise Ridge CTGD in the Getchell district. This study takes advantage of closely spaced underground and surface core holes that allow assessment of patterns around the HGB at an appropriate scale. By focusing on a single cross-section, we admit that the haloes around the HGB, which we discuss below, do not take into account the third dimension in and out of the plane of the section. In addition, there is no supergene oxidation in any of the holes in the cross-section, thus eliminat-

ing weathering as a possible explanation for any of the patterns presented below.

DISTRICT HISTORY

The Getchell district is located along the northeastern flank of the Osgood Mountains, 70 km northeast of Winnemucca, Nevada (Figures 1, 2). It includes the Getchell, Twin Creeks and Pinson mines, which have produced approximately 15.5 Moz of Au. The Getchell mine, which comprises several open pits along the Getchell fault, the Getchell underground deposit in the footwall of the Getchell fault, and the underground Turquoise

Ridge deposit in the hanging wall of the Getchell fault, has produced approximately 4.7 Moz of Au from ore containing an average grade of 10 g/t Au. At the end of 2009, proven and probable reserves were 10.7 million tons grading 17.4 g/t Au, almost entirely in the Turquoise Ridge deposit.

Getchell was discovered in 1934 and represents one of the first Carlin-type gold deposits mined in Nevada, 27 years prior to the discovery of the Carlin deposit. Open pit mining along the Getchell fault commenced in 1938 with the production of 788,875 ounces of Au, initially from oxide ores and then from sulfide ores, until reserves were depleted in 1951. Episodic exploration and mining continued throughout the property until 1983 when First Mississippi Corp. acquired Getchell, discovered 1,346,000 oz of minable reserves, and formed FirstMiss Gold to put the mine back into production in 1987, first from open pits and then from underground (Horton, 1999). In 1991 low-grade production of oxide ore from open pits in the Turquoise Ridge Oxide Zone commenced in the hanging wall of the Getchell Fault. Subsequent deep drilling below the Turquoise Ridge open pits penetrated high-grade sulfide ore. Continued drilling produced multiple high-grade intercepts resulting in the

sinking of a production shaft in 1996. In 1998 Placer Dome became the operator after a merger with Getchell Gold Inc, a subsidiary of FirstMiss Gold. Between 2001 and 2003, work focused on the development of the Turquoise Ridge North Zone. Underground production began in 2004 shortly after a joint venture between Placer Dome (75%) and Newmont Mining Corp. (25%) was established. Barrick Gold Corp. acquired Placer Dome in 2005 and currently operates the mine, which it now refers to as its Turquoise Ridge mine.

DISTRICT GEOLOGY

The geology of the Getchell mine area and the northern Osgood Mountains has been discussed in many publications (e.g., Joralemon, 1951; Hotz and Willden, 1964; Chevillon et al., 2000; Crafford, 2000; McLachlan et al., 2000; Boskie, 2001; Breit et al., 2005; Marlowe et al., 2007) and is summarized here. Ore bodies in the Getchell mine area are primarily hosted within a sequence of Cambrian-Ordovician carbonate and clastic rocks containing interlayered basalts that, in the past, have been mapped as Preble, Comus, and Valmy Formations

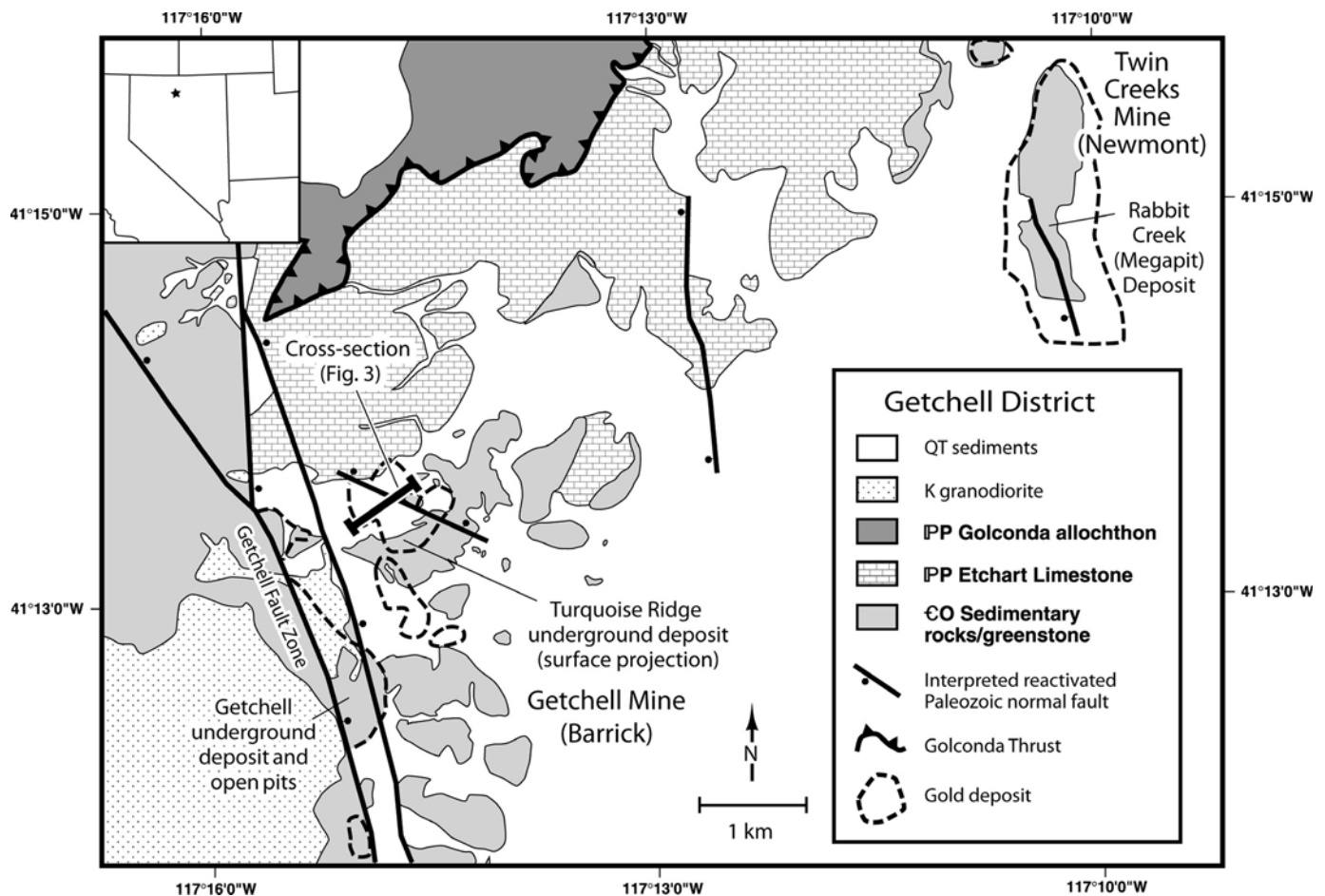


Figure 2. Simplified geologic map of the Getchell district (modified from Hotz and Wilden, 1964 and unpublished Placer Dome data). Shows trace of N55°E trending cross-section relative to the surface projection of the Turquoise Ridge underground deposit, Getchell underground deposit, and the Getchell open pits.

(lumped together as Cambrian-Ordovician rocks in Figure 2). Facies changes, gradational contacts, lack of age control, and lack of marker units in the mine area, discussed below, hamper assignment of these rocks into these established formations.

The primary ore-controlling structure in the district is the Getchell fault zone, which runs along the northeastern flank of the Cretaceous Osgood granodiorite stock. The fault zone dips between 30 and 80° east, mainly between 40° and 55°, and has a complex history with evidence for normal, reverse, and strike-slip motion. The Getchell fault and other faults highlighted in Figure 2 were proposed by Cline et al. (2005) and Muntean et al. (2007) to be Paleozoic normal faults that formed prior to the Late Devonian-Early Mississippian Antler Orogeny. They propose the Paleozoic normal faults are linked to underlying basement faults that originated during rifting of western North America during the Proterozoic.

The Cambrian-Ordovician rocks were complexly deformed, likely during the Antler Orogeny, prior to the deposition of the Pennsylvanian-Permian Etchart Formation. Basalt, chert, and siltstone, which have been historically assigned to the Valmy Formation, commonly have tight, locally recumbent, east to southeast-verging folds (e.g., Summer Camp Pit, Megapit at Twin Creeks) consistent with thin-skinned tectonics. On the other hand, the underlying rocks, which have more carbonate and have been traditionally assigned to the Preble and Comus Formations, commonly show west-verging more upright folds at Getchell and elsewhere in the Osgood and Edna Mountains (Madden-McGuire and Marsh, 1991; Crafford, 2000), including the Pinson Anticline at the Pinson mine, located just south of Getchell (McLachlan et al., 2000). These west-verging folds are also well expressed in seismic lines across the Getchell fault and its hanging wall (Cline et al., 2008). The west-verging structures are consistent with thick-skinned tectonics and are interpreted by Cline et al. (2005) and Muntean et al. (2007) to be the result of inversion of east-dipping normal faults, including the Getchell fault zone. The contact between the rocks historically assigned to the Valmy Formation and the underlying Preble and Comus Formations is locally expressed as a thrust fault that has been correlated with the Roberts Mountains thrust (e.g., Lopear thrust at Twin Creeks, Breit et al., 2005). However, in the Getchell mine area the thrust contact is not always apparent, the contact locally appears gradational, and no older-over-younger relationships have been documented, casting doubt whether it represents a regional thrust fault such as the Roberts Mountains thrust.

North of the Getchell mine area, the complexly deformed Cambrian-Ordovician sequence is unconformably overlain by the Pennsylvanian-Permian Etchart Formation, which is composed of variably sandy/silty limestone, calcareous siltstone/sandstone and conglomerate. Conglomerates with quartzite cobbles derived from the Cambrian-Ordovician sequence locally occur near the base of the Etchart, indicating a period of uplift and erosion after the Antler orogeny prior to or during the earliest deposition of the Etchart (Breit et al., 2005;

Muntean et al., 2007). The siliciclastic and basaltic rocks of the Mississippian-Permian Havallah Formation occur northwest of the Getchell mine area and were emplaced over Etchart Formation along the Golconda thrust during the late Permian to early Triassic Sonoma Orogeny. Broad, northeast-trending folds in the Etchart are interpreted to have occurred during the Sonoma and/or subsequent Mesozoic orogenies.

The Paleozoic rocks were intruded by the Cretaceous Osgood stock, which consists predominantly of medium-grained equigranular to porphyritic granodiorite and related dikes and sills of dacite porphyry, which were commonly emplaced along structures sub-parallel to the Getchell fault zone (Berger and Taylor, 1980). $^{40}\text{Ar}/^{39}\text{Ar}$ dates on hornblende and biotite indicate emplacement between 91 and 98 Ma (Groff et al., 1997). The contact metamorphic aureole extends up to 3 km from the stock and, in carbonate rocks, zones outward from calcite-wollastonite-diopside-garnet-tremolite skarnoids to marble. Siliciclastic rocks, depending upon the protolith, can contain cordierite, andalusite, muscovite, and/or biotite. Metasomatic skarn associated with the stock is expressed mainly by tungsten mineralization (scheelite) associated with andraditic garnet and iron-rich diopside and retrograde tremolite/actinolite-epidote-quartz-sulfides. Later and/or more distal metasomatic mineralization is expressed by quartz veins that contain variable amounts of carbonate, pyrite, pyrrhotite, arsenopyrite, and base metal sulfides. The Osgood stock appears to be part of a protracted magmatic-hydrothermal event ranging from 115-80 Ma based on $^{40}\text{Ar}/^{39}\text{Ar}$ dates and a U-Pb zircon date from Twin Creeks (Hall et al., 2000; Breit et al., 2005) and $^{40}\text{Ar}/^{39}\text{Ar}$ dates on hydrothermal K-feldspar and sericite at Getchell (Groff et al., 1997).

The Summer Camp, Hanson Creek, Getchell, and North open pits form a linear array of mined-out deposits along the Getchell fault. The Getchell underground development exploited ore in footwall splays and sympathetic fracture zones and dike contacts. The Getchell open pits and underground developments were within the contact metamorphic aureole of the Osgood stock, as defined by the presence of significant calc-silicates. The Turquoise Ridge oxide pits and the deep Turquoise Ridge refractory ore bodies occur in the hanging wall of the Getchell fault and straddle the margin of the metamorphic contact aureole. Mineralization at Turquoise Ridge extends discontinuously from the surface to a depth of over 1100 m. The main ore body plunges north, and the highest grades and tonnages are located at the north end at depths greater than 500 m. Ores in the Getchell district are largely devoid of supergene oxidation, which, although detrimental to economics, aids geologic studies. Gold grade is most closely correlated with the abundance of fine-grained gold-bearing arsenian pyrite associated with variable amounts of decalcification, argillization and silicification. Mineralization is Eocene in age, based on a 39.0 ± 2.1 Ma Rb-Sr age on galkhaite (Tretbar et al., 2000).

Present normal separation along the Getchell fault zone is indicated in the North pit by juxtaposition of basalts and cherts, historically assigned to the Valmy Formation, against limestone

and carbonaceous mudstone, historically assigned to the Comus and Preble Formations. Seismic data and limited drilling indicate apparent normal displacement could be as much as 300 m (Cline et al., 2008). How much of this normal movement is post-ore is uncertain; some of it could be synchronous with the deposition of the Etchart Formation (Muntean et al., 2007). However, post-ore movement on the fault is indicated by smeared orpiment and fine-grained pyrite along right-oblique and horizontal slickenlines (Boskie, 2001). Further post-ore normal movement is evidenced by steeply plunging slickenlines that overprint horizontal to very gently north- and south-plunging mullions and slickenlines. Post-ore rocks in the hanging wall of the Getchell fault include an Oligocene felsic tuff (27.1 ± 1.3 Ma, $^{40}\text{Ar}/^{39}\text{Ar}$, biotite, Ken Hickey, written communication, 2008), about 15 to 20 m thick, in the North Pit as well as alluvium up to about 5 to 10 m thick.

GEOLOGY OF THE NORTH END OF TURQUOISE RIDGE

The geology of the north end of the Turquoise Ridge deposit is characterized by a Cambrian-Ordovician sedimentary-volcanic package that has undergone a complex depositional, tectonic, metamorphic, and hydrothermal history. The complex depositional history of the package is compounded by rapid facies changes and a lack of marker units. Sediments within the deposit record multiple compressive and extensional deformational features, including both syn-sedimentary and tectonic. Pre-ore metamorphism related to the tectonic deformation and contact metamorphism and hydrothermal activity related to emplacement of the Osgood stock further hamper unraveling the geologic history. Given these complexities, understanding of the stratigraphy and structure of Turquoise Ridge continues to evolve.

The geologic framework presented here is based mainly on an underground cross-section that trends $N55^\circ E$ and cuts the north part of the Turquoise Ridge deposit through the HGB, the largest and highest-grade ore zone at Turquoise Ridge (Figure 2). The section was constructed from detailed logging of four surface diamond drill holes, spaced 60 m apart, and a fan of underground diamond drill holes (Figure 3). A color-coded logging scheme similar to that used by the Anaconda Company in the 1960s was employed, in which lithology, structure, alteration, vein types, and mineralization were graphically recorded at a scale of 1:120. The logging information was transferred by hand onto a 1:600 scale cross-section. Interpretive overlays were done by hand and then digitized using ArcGIS. The closely spaced drilling allowed for detailed interpretation. The lithologic units in Figure 3 represent a series of lithologic packages. Each of the individual lithologies described below can be seen in various proportions within each lithologic package. Unit designations at the deposit scale are assigned based on the most prominent rock types within a given unit.

The lowermost unit in the cross-section (unstippled purple

unit in Figure 3) is composed of carbonaceous mudstone and limestone (Figure 4A). The mudstone varies from siliceous and non-calcareous to argillaceous and variably calcareous. The carbonaceous mudstones are composed of quartz and/or calcite, muscovite (formed during metamorphism), biotite (formed during contact metamorphism), carbonaceous material (>0.5 wt % organic C based on downhole assays), minor pyrite, and trace pyrrhotite. The strata are commonly planar-laminated with local disruption of bedding, which presumably resulted from soft-sediment deformation. The limestone within this unit consists of dark grey to black recrystallized micrite containing variable amounts of quartz silt and organic carbon. Sporadic turbidite sequences up to tens of centimeters thick occur locally. The turbidites consist of graded beds of light grey, coarse-grained, recrystallized calcarenite.

A sedimentary breccia unit overlies the carbonaceous mudstones and limestones and contains similar lithologies as the lower planar sediments, but contains abundant breccias and features consistent with soft-sediment deformation that were later overprinted by tectonic deformation. The breccias consist of subrounded to subangular limestone fragments, supported by a carbonaceous, non-calcareous mudstone matrix (Figure 4 B-C). In thin section, the limestone fragments are composed of fine-grained, massive, recrystallized micrite, and the mudstone matrix is composed of unoriented muscovite and biotite, organic carbon, and trace pyrite. The limestone fragments commonly contain calcite veinlets that are truncated along the fragment margins. The unit is divided into a lower and upper member (Figure 3). The lower member consists of thick sections of limestone beds that have been stretched into disc-shaped clasts, which are typically several millimeters thick and several centimeters long (Figure 4B). The clasts can have consistent orientations in a given drill hole for several tens of meters. The disc-shaped clasts are interpreted to be parallel to bedding and are analogous to pinch and swell structures or boudins, which form in layers showing strong contrasts in ductility. In addition, the lower unit contains breccias with cm-sized limestone fragments that are commonly larger (up to at least 8 cm), rotated, and unoriented. The breccias in the lower member are difficult to correlate between drill holes, even between the closely-spaced underground holes in Figure 3. The upper member consists of about 70% breccia that is composed of finer-grained fragments than those in the lower member (Figure 4C). These upper, finer-grained breccias can commonly be correlated from hole to hole. The fragments are commonly elongated and oriented, and, the muddy matrix has a foliation, which in thin section, is accentuated by carbonaceous material. However, the foliation varies, and, in some thin sections, the muddy matrix has common tortuous whirls. None of the fragments contain recrystallized tails (i.e., pressure shadows) as would be expected if the breccias were related to brecciation during ductile, tectonic deformation. As pointed out by Muntean et al. (2007), the sedimentary breccia unit pinches out to the south, about 150 m south of the southeast corner of the cross-section in Figure 3.

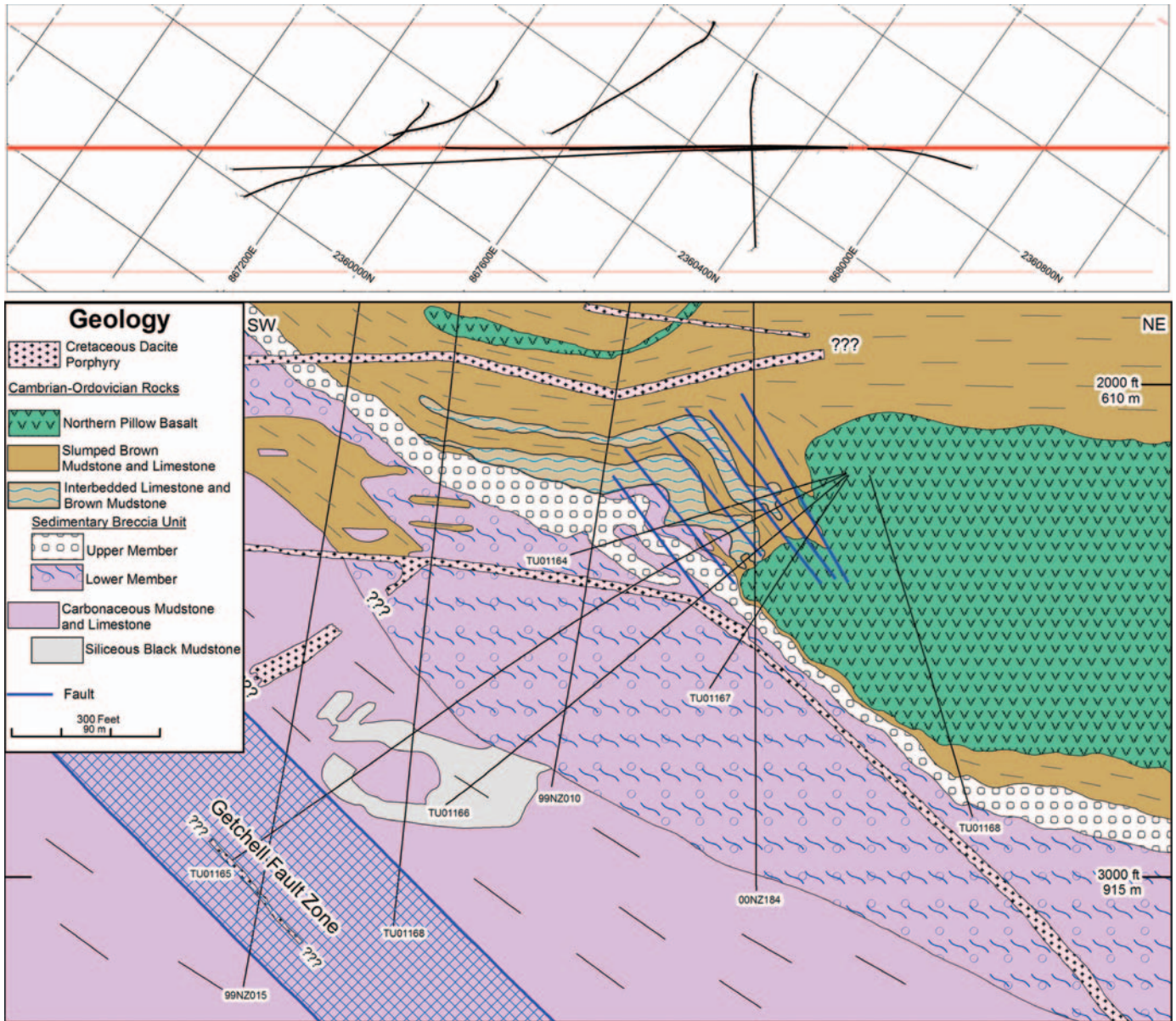


Figure 3. Underground cross-section through the Turquoise Ridge deposit oriented N55°E (section 3370, drill station 3). Shows the traces of the four surface core holes and five underground cores and interpreted geology. The top of the section is roughly 550 m below the surface while the bottom of the section is at a depth of approximately 975 m. The section's length is about 720 m. The panel above the cross-section is a map view, with a 60 m north-south grid, showing the surface projection of the traces of the holes relative to location of the cross-section (the red line in the center).

The pinch-out to the south has a fairly sharp margin that trends N80°W.

Above the sedimentary breccia unit lies a sequence of thin bedded, light grey, recrystallized micritic limestones and massive to poorly bedded, non-calcareous, brown mudstones containing less organic carbon content than the underlying carbonaceous mudstones (<0.2 wt % organic carbon) (Figure 4D). The brown mudstones contain foliated muscovite, unoriented biotite, and trace amounts of pyrite, pyrrhotite and rutile. The biotite, and possibly some of the muscovite, formed during contact metamorphism related to the emplacement of the Cretaceous Osgood stock and indicates a likely tuffaceous mudstone

protolith. The limestone beds are commonly complexly, ductilely folded. These folds are interpreted to be slump folds formed from soft-sediment deformation that were then variably overprinted by tectonic folding.

A thick section of basalt, referred to as the "northern pillow basalt" (NPB) overlies the sequence of deformed limestone and brown mudstone on the eastern half of the cross-section in Figure 3. The basalt is greenish gray, commonly aphanitic, and non-vesicular (Figure 4E). Pillow structures are locally abundant. The basalt contains tabular plagioclase phenocrysts that are commonly 0.2 to 1 mm in length. The fine-grained groundmass consists of primary orthopyroxene and magnetite

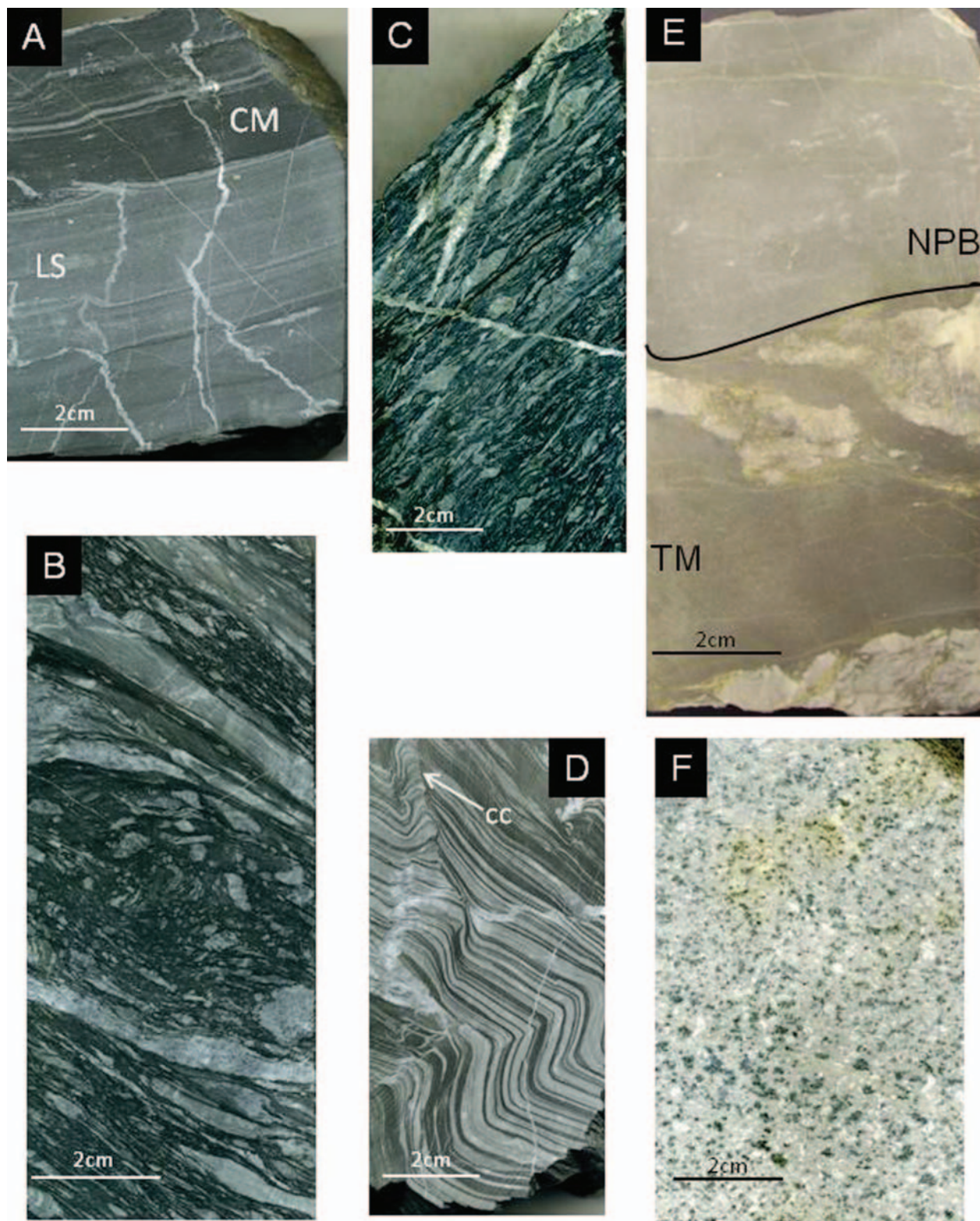


Figure 4. Sawed drill core of lithologies present at the north end of the Turquoise Ridge deposit. A. The lower interbedded carbonaceous mudstone (CM) and limestone (LS) unit (hole 99NZ015). B. Example of the lower member of the sedimentary breccia unit (hole TU01164A). C. Example of the upper member of the sedimentary breccia unit (hole TU01166). D. Interbedded brown tuffaceous mudstone and limestone showing complex folding overprinted by incipient crenulation cleavage (cc) (hole TU01164). E. Depositional contact between northern pillow basalt (NPB) and brown tuffaceous mudstone (TM) (hole TU01167). F. Least altered example of the main dacite porphyry dike (hole TU01167). Shows weak propylitic alteration characterized by the replacement of primary hornblende and biotite by chlorite and epidote and the replacement of plagioclase by albite and calcite.

that are partially to completely replaced by Fe-rich chlorite, epidote, and/or actinolite. The replacement of primary magnetite has resulted in a low, flat magnetic signature in surface magnetic surveys conducted at Turquoise Ridge (K. Wood, personal commun., 2008). Note the blunt southwestern margin of the NPB in Figure 3. The margin strikes N65°W, almost perpendicular to the cross-section. The contact between the NPB and underlying sediments is frequently broken, but is locally depositional (Figure 4E), suggesting that the basalt erupted onto the underlying sediments, rather than being tectonically emplaced.

Overlying the NPB are predominantly brown mudstones with thin, interlayered basalt flows and diabase sills, as well as minor limestone. Further upward and toward the present surface, above the cross-section in Fig. 3, basalt, tuffaceous siltstones and chert become more abundant with no definitive evidence for a major thrust fault as mentioned above. Overall, the carbonate and organic carbon content decreases upward in the stratigraphic section at Turquoise Ridge, whereas the volcanic component increases upward.

Features consistent with soft-sediment deformation and the southward linear pinch-outs of the sedimentary breccia unit and the NPB support the hypothesis originally proposed by Placer Dome geologists and published by Muntean et al. (2007) that there was a west-northwest trending active basin margin during deposition of the sedimentary host rocks at Turquoise Ridge. Based on bedding trends, the lowermost carbonaceous mudstones and limestones form a northwest-trending monocline that is interpreted to have originated by syn-depositional normal movement along a buried west-northwest-striking, northeast-dipping fault (Figure 2). The buried fault zone is interpreted to be linked to underlying basement rift faults of the same orientation that formed during the Proterozoic (Muntean et al., 2007). The normal faulting caused local topographic instability and the emplacement of slide blocks and sedimentary debris flow breccias, mainly of carbonaceous mud and partially lithified limestone. In addition, blocks of less carbonaceous limestone and brown tuffaceous mudstone slid northward over the breccia unit. Similar sedimentary debris flow breccias and slide blocks in Cambrian-Ordovician rocks have been documented in the Tybo district in the Hot Creek Range in central Nevada by Cook and Taylor (1977). Basalt then erupted and flowed up against the west-northwest-trending topographic barrier, forming the thick NPB. The submarine eruptions do not appear to have occurred along the basin margin, as evidenced by the lack of basaltic dikes in the vicinity of the margin. The transition from relatively deep quiet water sediments to disturbed sediments to volcanic rocks represents the onset of Cambrian-Ordovician extension in the Getchell area, which has been proposed for rocks of similar age in the Roberts Mountains Allochthon elsewhere in north-central Nevada (e.g., Madrid, 1987).

Rocks at Turquoise Ridge were later tectonically deformed by compression, primarily during the Antler Orogeny. The de-

formation is well-expressed in the cross-section in Figure 3 by a zone of folding along the blunt southwestern margin of the NPB. Several of the folds appear to be associated with west-northwest-striking, northeast-dipping, low-displacement faults along the margin. The faults now show either apparent normal or reverse separation. The blunt southwestern margin of the thick NPB reflects a major competency contrast with the surrounding mudstone and limestone. Similar compressional deformation is seen in a diabase sill overlying the brown mudstones and limestones, near the top and just above the cross-section in Figure 3. A definite tectonic cleavage is variably developed in the rocks at Turquoise Ridge. It occurs as a spaced crenulation cleavage that is generally oriented at a high angle to bedding (Figure 5A). The crenulation cleavage is defined by sub-parallel wispy planes of carbonaceous material (Figure 5B) and muscovite as well as kinking of muscovite grains in some samples.

Figure 6 schematically illustrates our interpretation of the development of the Cambrian-Ordovician basin margin and its subsequent deformation during the Antler Orogeny. The contact between the NPB and underlying sediments was originally a depositional contact, representing an angular unconformity of about 20°. This suggests the underlying sediments were tilted up to 20° during the formation of the extensional monocline. Basalt then flowed up against the steepened slope and inter-fingered with brown mudstone and limestone toward the top of the basalt. During the Antler and subsequent orogenies, the angular unconformity between the NPB and the underlying sediments significantly steepened near the margin of the NPB. The sediments along the margin of the competent basalt took up the strain by folding like an accordion, whereas strain in the basalt was accommodated by minor thrust faults.

Cretaceous dacite dikes intrude the Cambrian-Ordovician rocks in the cross-section in Figure 3, and throughout Turquoise Ridge. A prominent dike transects the entire cross-section in Figure 3 and varies between 4 and 11 meters in thickness. This “main dike” strikes sub-parallel to the Getchell fault, and its dip decreases significantly to the southwest. Zircons from the main dacite dike have given a U-Pb age of 115 ± 2.3 Ma (Ken Hickey, written communication, 2008), which is older than the Osgood stock, but similar in age to a dacite porphyry dike at Twin Creeks (Breit et al., 2005). The least altered samples of the main dacite porphyry dike contain plagioclase phenocrysts (0.2–1.0 mm) and lesser biotite and hornblende phenocrysts (0.1–0.2 mm) set in a very fine-grained (<0.1 mm) groundmass of quartz, plagioclase, minor hornblende and biotite, and trace magnetite and zircon (Figure 4F).

Abundant high-angle faults and fracture zones with variable orientations are located throughout the Turquoise Ridge deposit. The vast majority of the faults in the underground workings lack continuity along strike and down dip. The faults typically have apparent normal displacements of less than 5 meters and are very difficult to correlate between holes. Thus, none of these faults are shown in Figure 3. Based on alteration and gold grade patterns

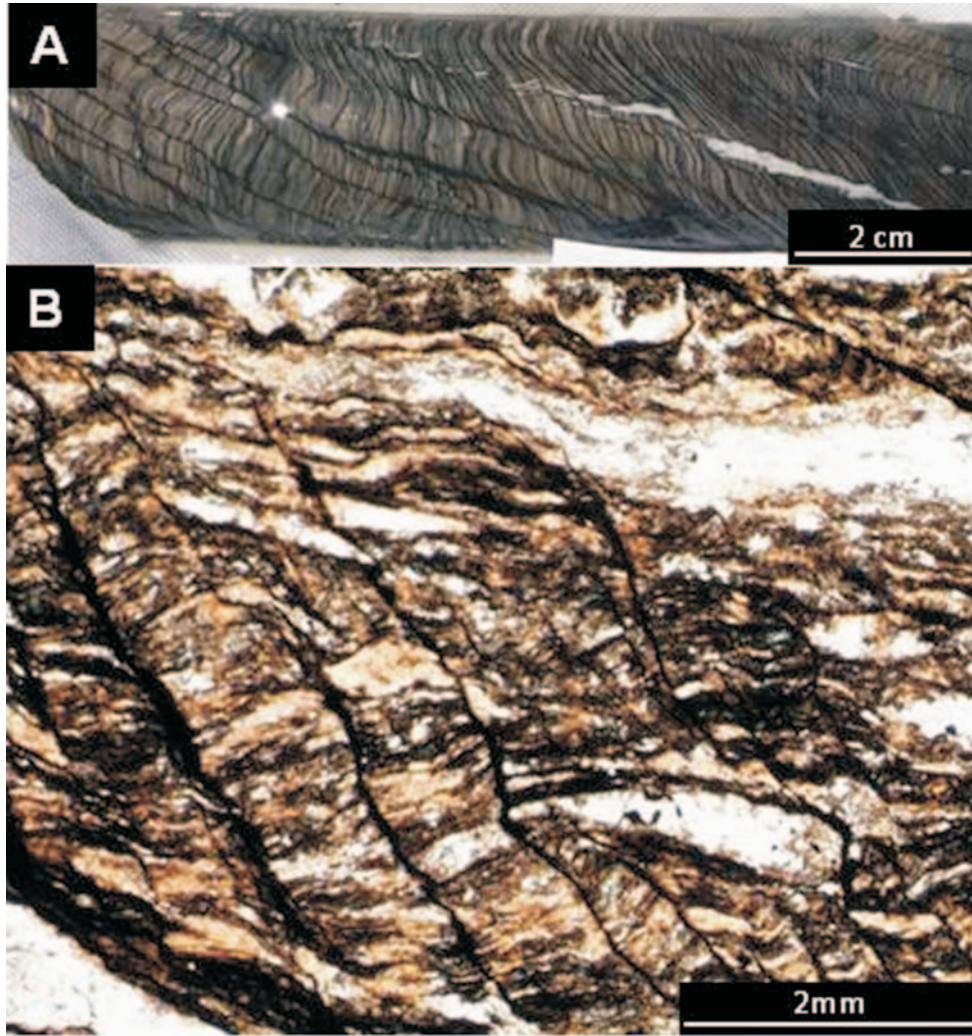


Figure 5. Examples of crenulation cleavage. A. Cleavage at high angle to bedding (sawed drill core, hole 00NZ135, located very close to cross-section in Fig. 3). B. Thin section photomicrograph showing cleavage defined by wispy planes of carbonaceous material (hole TU001165).

discussed below, numerous steep, small-displacement antithetic faults occur on the west side of the cross-section in the hanging wall of the Getchell fault. Drill intersections of the Getchell fault in Figure 3 show it to be an approximately 140 m thick zone composed of an elaborate fracture network represented by closely spaced, often overlapping, broken zones that show evidence for variable fault movement. The broken zones vary from gouge to rubble with locally preserved slickenlines along graphite(?) coated fracture surfaces. The drill intersections show similar-looking carbonaceous mudstones and limestone on both sides of the fault, which argues against large-scale net displacement along the Getchell fault.

ALTERATION AND GOLD MINERALIZATION

Currently-defined ore zones at Turquoise Ridge occur within a north-plunging mineralized zone roughly 1,000 meters (N-S) by 600 meters (E-W) (Chevillon et al, 2000). Gold miner-

alization follows a N30–40°W fabric that is sub-parallel to the Getchell fault. The ore zones within the Turquoise Ridge deposit occur along complex intersections between: 1) northeast to northwest-trending, high-angle small-displacement faults and fracture zones, 2) the west-northwest-trending Paleozoic basin margin, 3) synforms and antiforms, and 4) calcareous lithologies (Muntean et al., 2009). The alteration and mineralization patterns at the north end of Turquoise Ridge, discussed in this paper, are based on the detailed underground cross-section in Figure 3. Decalcification, argillization, and silicification are the alteration features most closely associated with gold mineralization at Turquoise Ridge and are the result of interaction of an acidic hydrothermal fluid with the host rocks. Decalcification occurred where acidic fluids reacted with calcareous lithologies, such as calcareous mudstone and recrystallized micritic limestone, as well as quartz+carbonate veins associated with the emplacement of the Osgood stock. Such decalcified veins commonly have vugs lined with pre-ore,

ate within the rock. Figures 7A-B show unaltered, finely interbedded, recrystallized micritic limestone and mudstone. The limestone layers are typically composed of fine-grained subhedral calcite grains (<0.01–0.1 mm) along with minor quartz-silt (<0.01 mm) and diagenetic pyrite (<0.1 mm). In strongly decalcified/silicified samples of similar interlayered limestone and mudstone (Figures 7C-D), hydrothermal quartz grains (<0.01mm) have completely replaced calcite grains, leaving a delicate sponge-like texture with about 20–40% pore space. Gold-bearing arsenian pyrite or marcasite occur along the boundaries of the hydrothermal quartz grains and are intergrown with kaolinite and/or illite as detailed below. The contemporaneous association between Au-bearing arsenian pyrite/marcasite and hydrothermal quartz (jasperoid) indicates that these minerals formed during a single hydrothermal event. In addition, the hydrothermal quartz exhibits primarily a reticulate texture that has been interpreted to represent formation at temperatures greater than 180°C (Lovering, 1972; Dong et al, 1995). Such rock could very well scratch by fracturing the delicate sponge-like quartz framework, and most field geologists would log such alteration as decalcification, despite the abundance of quartz. Cline (2001) referred to such alteration at the Getchell deposit as jasperoid, which it technically is. However, field geologists in Nevada typically log rocks as jasperoid only if it leaves steel upon scratching, that is, rocks are completely silicified and lack the sponge-like textures of incompletely silicified, decalcified rocks. Such dense jasperoid was only locally logged during this study.

Figure 8A shows the interpreted pattern of ore-stage hydrothermal alteration along the detailed cross-section. Because they both resulted from interaction of acidic fluids with the country rocks, decalcification, silicification and argillization were lumped together into the following categories: 1) moderate to strong alteration consisting of lithologies having rock textures that are commonly (but not always as demonstrated in Figure 7) destroyed and have little to no reaction with 5% HCl and, 2) weak to moderate alteration consisting of wall rocks having moderate to strong bleaching, largely preserved rock texture, and weak to moderate reaction with 5% HCl. Outside the alteration zones shown in Figure 8A, rocks either show no visible, megascopic alteration or contain local, narrow alteration zones that were too sporadic and widespread to be contoured. Note that weak to moderate alteration does not form a halo to moderate to strong alteration throughout most of the cross-section. Visually unaltered rock commonly occurs adjacent to moderately to strongly altered rock. The outer margins of the main dacite dike are almost everywhere argillized. Moderate to strong alteration occurs in the footwall and hanging wall of the dacite dike, extending into the folded sediments adjacent to the blunt edge of the NPB. In addition, weak to moderate alteration extends well into the hanging wall and footwall of the main dacite porphyry dike in the eastern portion of the cross-section. The Getchell fault zone in the lower, southwest corner of the section consists of a narrow central zone containing strong alteration that is surrounded by a broad zone of

weak to moderate alteration. Similarly, weak to moderate or moderate to strong alteration is interpreted to occur along the high-angle, west-dipping antithetic fault zones that extend upward from the Getchell fault zone. The largest alteration zone occurs where these antithetic structures intersect the footwall of the dacite dike within the sedimentary breccia unit. Although some of the antithetic fault zones can be traced across the dike, alteration appears to persist along only a few of them.

Late ore-stage realgar and orpiment mineralization, consistent with what Cline (2001) reported for the Getchell deposit, was logged. Realgar is slightly later paragenetically and is much more abundant than orpiment. The abundance of realgar progressively increases along the cross-section from northeast to southwest and primarily occurs in the footwall of the main dacite dike (Figure 8B). Though spatially related to ore, its distribution does not form a consistent pattern with respect to ore, mainly because it is paragenetically later than the Au. Also, the abundance of calcite veins, which were logged in detail, shows no spatial pattern with respect to ore or alteration.

Gold assays of drill core intervals that were up to 1.5 meters in length were plotted using Target software, an add-on for ArcGIS developed by Geosoft and hand-contoured using the following intervals: 1) ≥ 0.34 ppm, 2) ≥ 3.4 ppm, and 3) ≥ 17 ppm (Figure 8C). The Au grades commonly show abrupt variations, locally changing from ≥ 17 ppm to < 0.34 ppm within meters. The HGB is represented by the large zone of ≥ 3.4 ppm Au that occurs at the intersection of the main dacite dike and the steep antithetic faults that extend upward from the Getchell fault zone. The HGB extends over 60 meters into the footwall of the dacite dike within the lower member of the sedimentary breccia unit and 105 meters into the hanging wall within the upper member of the sedimentary breccia unit and the folded brown mudstones and limestones adjacent to the blunt edge of the NPB. Gold grades ≥ 17 ppm extend up to 20 meters into the footwall of the dacite dike within the central portion of the HGB and extend up to 75 meters into the hanging wall of the dike. The high-grade zones in the hanging wall are commonly lenticular bodies that are discordant to bedding and occur along the thrust faults associated with the folded sediments adjacent to the NPB. Pervasive Au grades ≥ 3.4 ppm within the HGB extend up to 40 meters above and 55 meters below the zone of ≥ 17 ppm Au. Zones of ≥ 0.34 ppm Au extend up to 120 meters above and up to 150 meters below the HGB, occur within the Getchell fault, and occur along several steep, small-displacement, antithetic faults in the hanging wall of the Getchell fault. Attempts were made to contour Au grades of ≥ 0.10 ppm, ≥ 0.05 ppm, and ≥ 0.025 ppm in order to evaluate whether they form broader haloes to the 0.34 ppm Au contour. Gold assays of ≥ 0.05 ppm locally extend up to 15 meters beyond the 0.34 ppm Au contour; however, such low grades lack sufficient continuity to contour at the scale of the cross-section in Figure 8C.

Gold grades of ≥ 0.34 ppm display a strong spatial correlation with moderate to strong alteration. Weak to moderate alteration extends locally up to tens of meters beyond the ≥ 0.34 ppm

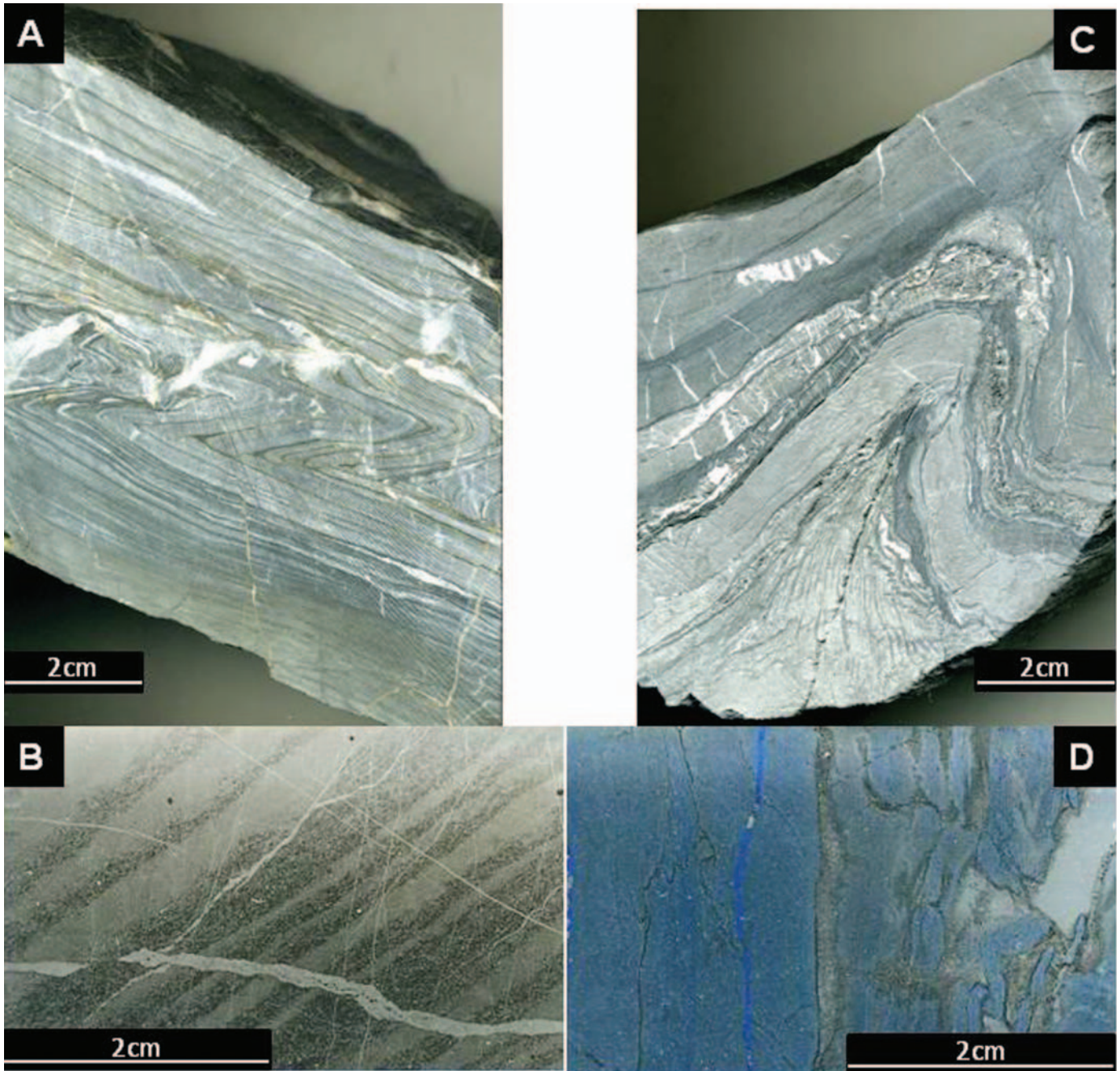


Figure 7. A. Unaltered, folded, finely laminated recrystallized micritic limestone (gray) and brown mudstone (hole TU01166). B. Thin section of unaltered finely laminated micritic limestone (light layers) and mudstone (dark layers) (hole TU01165). Note the preservation of primary rock fabric despite the total dissolution of carbonate. C. Strongly decalcified, laminated limestone and mudstone that is very similar to A (hole TU01165). D. Thin section of strongly decalcified, laminated limestone and mudstone that is very similar to C (hole TU01165). Note the increase in porosity in D relative to B, as represented by the abundant blue epoxy in D. The bluish layers in D were limestones in which the calcite has been completely dissolved. The limestone layers are now a delicate sponge-like framework of quartz and very fine-grained pyrite and marcasite.

Au contour, such as in the Getchell Fault zone, in the footwall of the dacite dike below the central part of the HGB, and in the folded brown mudstones and limestones adjacent to the NPB. The strong spatial correlation between gold grade and alteration suggests wall rock alteration occurred contemporaneous with gold mineralization.

Because much of the gold and alteration appear to be associated with fault and fracture zones, values of rock quality designation (RQD) were plotted and contoured to determine the relationship between gold grade and rock fracture density (Figure 8D). Zones of high fracture density could be reflecting zones of greater permeability and paleo-fluid flow. Very poor RQD val-

ues of less than 25% (>150 fractures per 3m interval) coincide with the Getchell fault zone. The RQD values also show a broad halo of fractured rock around the narrow visible alteration zones associated with the steep antithetic faults in the hanging wall of the Getchell fault. Similarly, low RQD values exist in the hanging wall and footwall of the main dacite dike and extend into the folded tuffaceous mudstones and limestones adjacent to the NPB. There are very few areas along the cross-section where anomalous Au-values (≥ 0.34 ppm Au) are present in rocks having RQD values greater than 50%. The RQD distribution supports our interpretation that ascending ore fluids exploited pre-existing fault and fracture zones rather than being bound to specific stratigraphic horizons. Also the association with low RQD values with ore and alteration could be the result of fracturing caused by collapse during carbonate dissolution associated with ore formation.

MULTI-ELEMENT DATA

The statistics and distribution of downhole multi-element

analyses, provided by Barrick, were evaluated along the detailed cross-section in order to assess dispersion haloes around the HGB ore zone. Barrick's downhole sampling of visually unaltered rock within the five underground drill holes was limited to 6 meters above and below visual alteration zones. Analyses of 50 elements were completed by ALS Chemex utilizing a nitric aqua regia digestion followed by analysis by ICP-MS-AES (ALS Minerals ME-MS41). Elements that are not completely digested by nitric aqua regia include Al, Ba, Be, Ca, Cr, Ga, K, La, Na, Sr, Ti, and W. The data were combined with the Au assays collected from the same drill interval. Multi-element data from surface holes analyzed by Placer Dome were composite samples from 3 m intervals. They are ICP-AES analyses that were completed by American Assay Laboratories using an aqua regia digestion. Analyses that contained values less than the detection limit for a given element were given a value of half the detection limit prior to statistical analysis and plotting. Statistical analyses, including descriptive statistics, Pearson correlation coefficients, Spearman rank correlation, and traditional R-mode factor analysis, were limited to analyses of the five un-

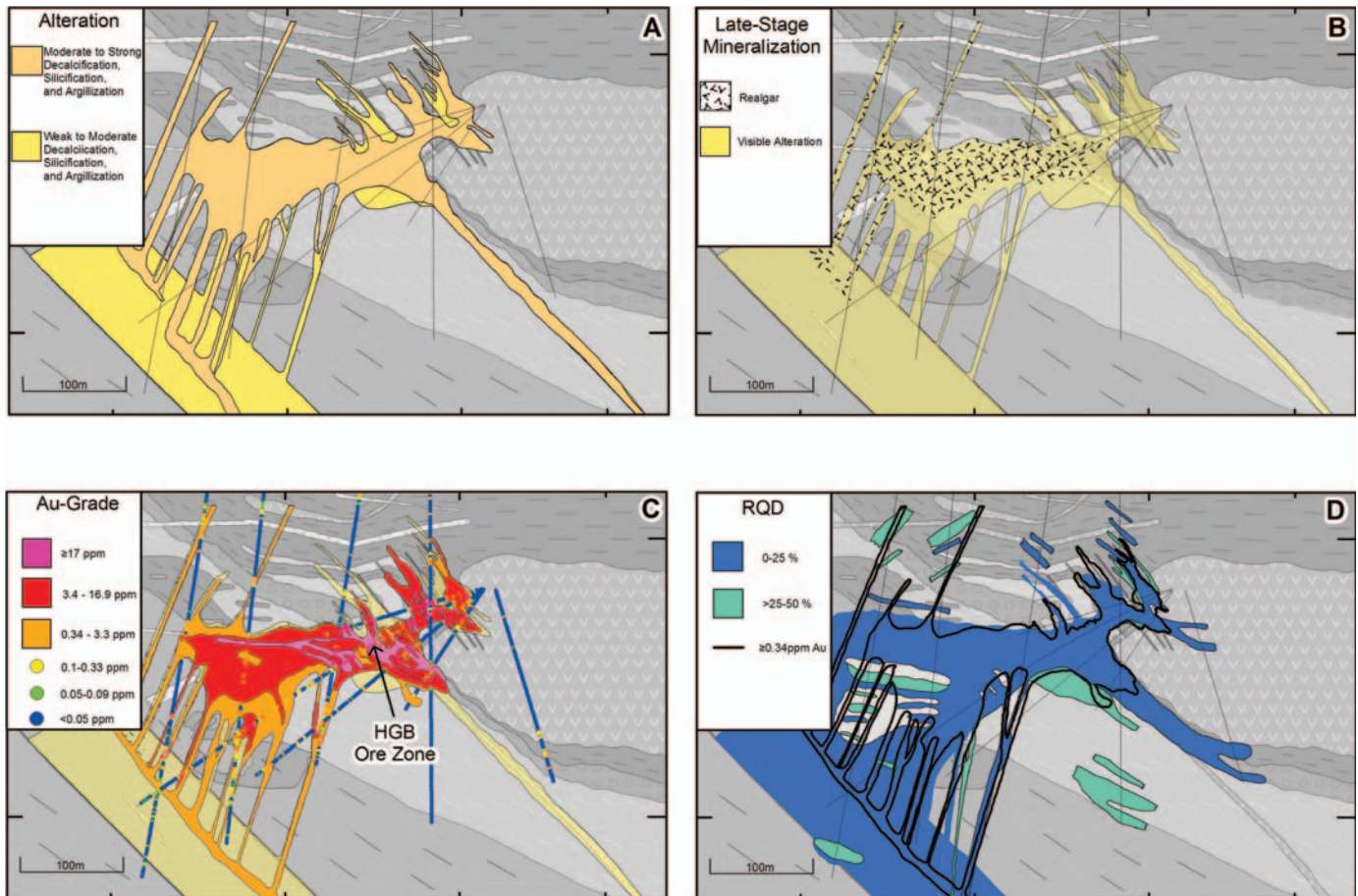


Figure 8. A. Distribution of hydrothermal alteration related to ore formation. B. Late-stage realgar mineralization. C. Au-grade contours showing high (≥ 17 ppm Au, magenta), moderate (≥ 3.4 ppm, red), and low (≥ 0.34 ppm, orange) grades in relation to alteration (yellow). Note the individual assays of drill intervals, represented by points along individual drill holes. D. Distribution of RQD, which was determined by the sum of the lengths of core longer than 10 cm divided by the total length of core multiplied by 100 for a given interval of core. Points represent individual RQD determinations for drill intervals.

derground drill holes. Statistical analyses were carried out using the software package SYSTAT 11. Trace element analyses from the four surface holes cover the entire length of the holes, but were excluded from the statistical analysis because of the differences between the older American Assay analytical package and the newer ALS Chemex package. Also, the detection limits were higher for several of the elements in the American Assay package.

Statistics

Pearson correlation coefficients were calculated to determine which trace elements correlate linearly with gold. Gold strongly correlates with Tl ($r = 0.765$), Hg ($r = 0.701$), and As ($r = 0.611$) and more weakly with Te ($r = 0.588$), Sn ($r = 0.556$), and In ($r = 0.502$). Spearman rank correlation coefficients were also calculated and are preferred because the method does not depend upon linear relationships and is less influenced by outliers. The Spearman rank correlation matrix for 18 of the elements, along with accompanying scatter plots, is presented in Figure 9. Gold shows a strong positive correlation with Hg ($r = 0.889$), As ($r = 0.849$), W ($r = 0.819$), S ($r = 0.783$), Tl ($r = 0.78$), and a weaker correlation with Sb ($r = 0.671$), Te ($r = 0.616$), In ($r = 0.598$), and Sn ($r = 0.575$). Gold displays a strong negative correlation with Mg ($r = -0.727$), Ca ($r = -0.677$), and Sr ($r = -0.69$).

Traditional R-mode factor analysis was conducted utilizing a varimax rotation and minimum eigen value of 1.00. Varimax rotation was utilized to maximize the variance that each factor symbolizes (Abdi, 2003). Because most of the elements showed log-normal distributions, the log values for each element were used for the factor analysis, because factor analysis is based on the assumption of normal populations. Table 1 displays the six calculated factors and the associated factor loadings for the entire geochemical database. The six factors account for nearly 80% of the variance in the data set.

Factor 2, which explains nearly a quarter of the variance, is the factor mostly closely associated with Au mineralization. The highest loadings for Factor 2 are Au (0.922), Hg (0.906), As (0.879), W (0.864), S (0.813), Tl (0.734), Sb (0.712), Te (0.646), In (0.619), Sn (0.590), and Pb (0.507), an elemental suite similar to the one determined by the correlation coefficients. Conversely, negative loadings for Factor 2 include Mg (-0.844), Ca (-0.823), Sr (-0.796), and Mn (-0.791), again a suite similar to the one determined by the correlation coefficients. The five other factors all have very low loadings for Au. Factor 3 explains nearly 18% of the variance. The elements with high loadings in Factor 3 are Co, Fe, Ge, Ga, Sc, Y, Al, Ta, V, In, Ti, Li, Zn, Sn, Be, and Ni. These elements are interpreted to represent an igneous rock signature, including both the mafic Cambrian-Ordovician basalts and the felsic Cretaceous granitic intrusions. Elements with high loadings for Factor 4 include Re, P, Mo, Cu, Ag, Se, Cd, Hf, Zr, U, Nb, V, and Sb. This elemental association, which explains nearly 17% of the variance, is inter-

Table 1. RESULTS OF FACTOR ANALYSIS SHOWING LOADINGS FOR 6 FACTORS.

	Factor 1	Factor 2	Factor 3	Factor 4	Factor 5	Factor 6
Ag	0.047	-0.086	-0.227	0.848	0.148	-0.013
Al	0.326	-0.445	0.663	-0.280	-0.259	-0.188
As	0.106	0.879	-0.003	-0.040	-0.018	0.051
Au	0.095	0.922	-0.017	-0.026	0.034	0.068
B	0.331	0.066	-0.114	-0.252	-0.182	0.400
Ba	0.461	-0.669	-0.150	0.127	0.073	-0.092
Be	0.312	-0.113	0.477	-0.422	-0.478	0.168
Bi	0.556	0.296	-0.121	0.194	-0.279	0.059
Ca	-0.036	-0.823	-0.248	0.241	0.138	0.331
Cd	-0.020	-0.017	-0.390	0.819	0.051	0.142
Cd	0.052	0.195	0.035	-0.376	-0.807	-0.008
Co	0.050	0.206	0.904	-0.258	0.011	-0.005
Cr	0.349	-0.263	0.140	0.104	-0.605	0.012
Cs	0.750	0.098	0.307	-0.269	-0.154	0.149
Cu	0.034	0.194	0.128	0.865	0.098	0.026
Fe	0.059	0.355	0.863	-0.185	0.072	-0.032
Ga	0.242	-0.267	0.811	-0.270	-0.199	-0.209
Ge	0.032	0.152	0.853	-0.120	-0.100	-0.142
Hf	0.075	-0.178	0.085	0.676	-0.425	-0.339
Hg	0.098	0.906	-0.231	0.084	-0.018	0.157
In	0.226	0.619	0.610	-0.029	0.083	0.042
K	0.773	-0.208	0.002	-0.157	-0.478	-0.045
La	0.070	0.178	-0.097	-0.328	-0.834	0.014
Li	0.146	-0.388	0.557	-0.332	-0.466	-0.106
Mg	0.274	-0.844	0.243	-0.154	0.053	0.144
Mn	0.031	-0.791	0.003	0.141	0.341	0.291
Mo	-0.102	-0.015	-0.315	0.866	0.053	0.036
Na	0.392	-0.601	0.278	-0.121	0.091	-0.231
Nb	-0.037	-0.285	0.120	0.449	0.140	-0.292
Ni	0.184	0.346	0.410	0.258	-0.552	0.227
P	-0.203	-0.079	-0.074	0.866	0.126	-0.127
Pb	0.237	0.508	0.053	0.159	-0.481	0.111
Rb	0.738	-0.164	0.109	-0.164	-0.531	-0.053
Re	-0.151	0.046	-0.155	0.893	0.132	0.029
S	-0.129	0.813	0.165	0.187	-0.081	0.097
Sb	0.033	0.712	-0.077	0.404	0.254	0.111
Sc	-0.006	-0.274	0.756	-0.373	0.037	0.292
Se	0.019	0.200	-0.177	0.846	0.111	0.105
Sn	0.325	0.590	0.526	-0.149	-0.152	0.002
Sr	-0.001	-0.796	-0.332	0.151	0.101	0.308
Ta	-0.214	-0.047	0.651	-0.018	0.345	-0.146
Te	0.456	0.646	-0.345	0.242	0.152	0.085
Th	0.319	0.225	-0.325	-0.198	-0.786	0.078
Ti	0.223	-0.646	0.604	-0.117	0.124	-0.268
Tl	0.449	0.734	-0.237	0.149	0.085	-0.009
U	0.021	0.066	-0.587	0.539	-0.463	0.050
V	-0.106	-0.535	0.630	0.431	0.173	-0.048
W	-0.096	0.864	0.057	-0.021	0.001	0.181
Y	-0.339	-0.287	0.745	0.005	0.022	0.119
Zn	-0.055	0.218	0.537	0.361	-0.151	0.206
Zr	0.067	-0.042	-0.052	0.611	-0.553	-0.335
%Var	8.08	23.53	17.57	16.82	10.52	2.88

Loadings that are 0.4 are shown in bold typeface. Var=variance.

preted to represent a black shale or basinal fluid flow signature that formed prior to ore formation. A similar signature has been documented at Jerritt Canyon (Hofstra, 1994, Patterson, 2009) and other CTGDs (cf. Sha, 1993; Emsbo et al., 1999). Factor 1

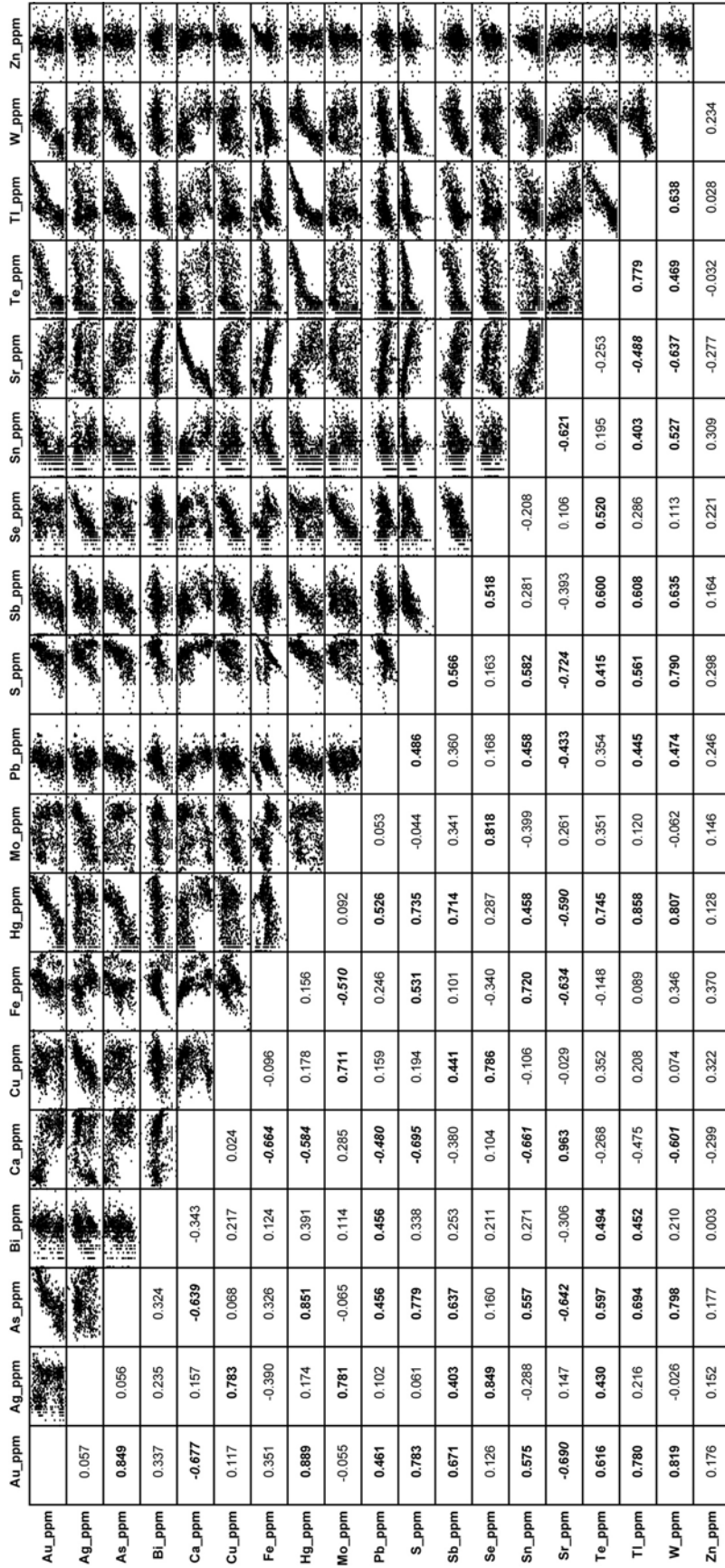


Figure 9. Correlation matrix of 18 selected trace elements based on analyses of ≤ 1.5 m drill hole intervals from the five underground drill holes. Shows Spearman rank correlation coefficients and accompanying scatter plots. Correlation coefficients that are >0.4 and <-0.4 are in bold and bold italics, respectively.

explains 8% of the variance and elements and has significant loadings for K, Cs, Rb, Bi, Ba, Te, and Tl. This elemental association might be related to mineralization associated with the Osgood stock. The remaining Factors 5 and 6 do not contain high factor loadings for any of the elements and are considered to be geologically insignificant.

Distribution of Ore-Related Trace Elements

The Barrick and Placer Dome data sets were utilized to investigate the distribution of ore-related trace elements relative to Au assays and visible alteration. We focused on Hg, Sb, As, Te, and Tl, which were the main elements related to gold deposition as determined by the correlation coefficients and factor analysis (i.e., Factor 2). These five trace elements are commonly present in ore-stage, Au-bearing arsenian pyrites from the Getchell and Turquoise Ridge deposits, based on electron probe microanalyses (Cline, 2001; Longo et al., 2009) and, therefore, their distribution is interpreted to be the result of the Eocene Au-mineralization event. The values of these elements were plotted down the drill holes using Target and were compared to estimated background values (Table 2). Histograms of individual elements were used to locate breaks in the data distribution in order to classify the values for contouring. The values of Hg, Sb, and As, from the Placer Dome surface holes and the Barrick underground holes were hand-contoured (Figure 10), whereas Te and Tl from only the underground holes were plotted (Figure 11).

The spatial distribution of Hg is similar to that of Au (Figure 10A). The 1 ppm Hg contour closely mimics the 0.34 ppm Au contour on the cross-section, and the 10 ppm Hg contour is very similar to the 3.4 ppm Au contour. Zones of >100 ppm Hg are almost entirely limited to within the 17 ppm Au contour. Overall Hg is concentrated in the zone of antithetic faults between the Getchell fault and the HGB ore zone. Within the Getchell fault zone, Hg values ≥ 1 ppm are limited to narrow intercepts that are 3–12 meters thick. Elevated Hg values above the inferred background average (>0.04 ppm, Table 2) extend no more than 10 meters beyond visibly altered wall rocks and the ≥ 0.34 ppm Au contour based on the underground holes. However, understanding of the overall pattern of ppm Hg, especially above the HGB, is hampered by a <1 ppm detection limit for the Hg analyses in the Placer Dome surface holes.

Antimony values are consistently above an inferred background of 0.5 ppm (Table 2) in all of the holes (Fig. 10B). Sb values ≥ 5 ppm commonly form haloes up to 12 meters beyond the ≥ 0.34 ppm Au contour throughout the Getchell Fault zone, the zone of antithetic faults zone below the HGB ore zone, and in the deformed brown mudstones and limestones adjacent to the NPB above the HGB. The 25 ppm Sb contour mimics fairly closely the 3.4 ppm Au contour. The largest zone of ≥ 25 ppm Sb occurs in the lower parts of the HGB in the footwall of the main dacite dike in the zone of antithetic faults.

Arsenic forms a slightly larger, more continuous halo around Au mineralization than does Hg or Sb (Figure 10C). Ar-

senic values of ≥ 100 ppm are broadly coincident with visibly altered rocks within the Getchell fault zone but extend beyond visible alteration and the 0.34 ppm Au contour in the antithetic fracture zone, forming a wide zone of ≥ 100 ppm As below the HGB. Persistent As values of ≥ 100 ppm extend up to 30 meters beyond visible alteration and the 0.34 ppm Au contour along the thrust faults adjacent to the NBP. The 1000 ppm As contour is broadly coincident with the 3.4 ppm Au contour.

The distribution of anomalous Tl, based on the five underground holes, is similar to that of Au (Figure 11A). Tl values of >5 ppm are mostly restricted to zones of ≥ 3.4 ppm Au in the central core of the HGB ore zone. In the upper parts of the HGB, within the deformed mudstones and limestones adjacent to the NPB, Tl values are mainly <5 ppm even in zones of >3.4 ppm Au. Tl values of >0.5 ppm, which is greater than the inferred background of 0.15 ppm (Table 2), commonly extend up to about 10 meters beyond visible alteration and the >0.34 ppm Au contour. The Tl values in the Getchell fault zone are mainly <0.5 ppm.

The distribution of anomalous Te, based on the five underground drill holes, is more restricted than Au (Figure 11B). Te values of 1 ppm are almost entirely confined to the central core of the HGB ore zone. In the upper parts of the HGB, Te values decrease to mostly <0.1 ppm, which is near the inferred background (≥ 0.08 ppm, Table 2), even in areas of ≥ 3.4 ppm Au. Te values are fairly consistently ≥ 0.1 ppm in the zone of antithetic fracture zones just below the HGB; however, the values are mainly <0.1 ppm in the Getchell fault zone.

Factor scores for Factor 2 (the Au factor discussed above, Table 1) were calculated for each sample from the underground data set by summing the products of the concentration and Factor 2 loading for each element. The scores for each sample were then plotted on the cross-section (Figure 11C). Plotting gold factor scores on cross-sections or on maps enables one to seek out zones of high statistical association between Au-related trace elements, even in the absence of high Au values. For example, if As, Hg, Sb, Tl, and Te values are high in a given area where Au values are low, high Au factor scores may still be present. Figure 11C shows high Factor 2 scores (≥ 0.8) strongly correlate spatially with the ≥ 3.4 ppm Au contour. Unfortunately, the factors scores outside the ≥ 3.4 ppm Au contour do not show a consistent pattern. Likewise, Factor 2 scores of <0.8 do not show any pattern in relation to either altered or unaltered rock.

Sulfidation

Gold primarily resides in trace element-rich arsenian pyrite, arsenian marcasite, or arsenopyrite in most CTGDs (cf. Hofstra and Cline, 2000). The gold-bearing pyrite at the Getchell and Turquoise Ridge deposits occurs as micron-sized, fuzzy, spheroidal grains or as micron-sized rims on trace element-poor, pre-ore pyrite (Cline, 2001; Longo et al., 2009). Based on electron microprobe analyses, the trace elements enriched in this ore-stage pyrite include Au, As, Hg, Sb, Tl \pm Te \pm Cu (Cline et al., 2005; Longo et al., 2009). Thus, the amount of

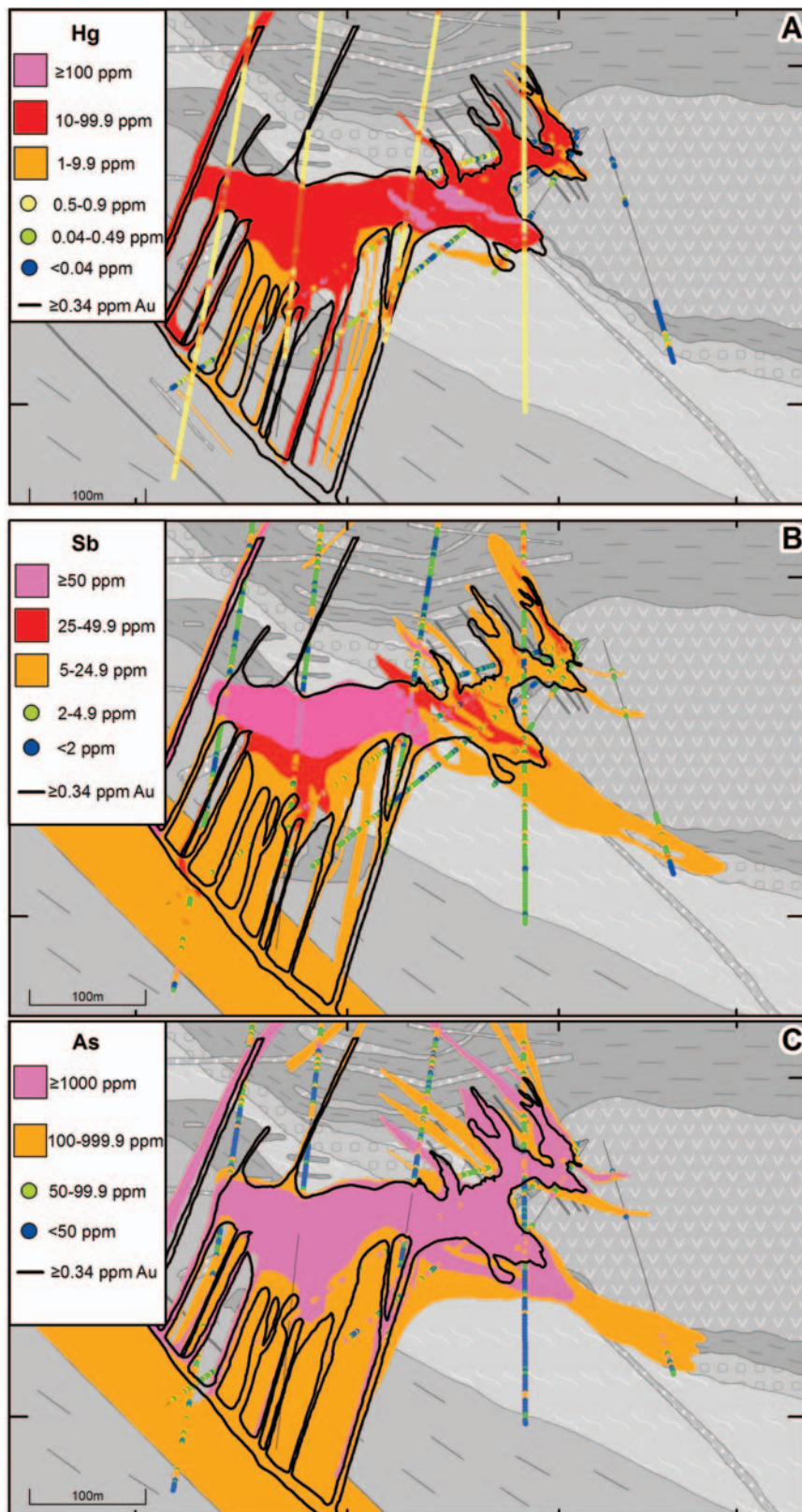


Figure 10. A. Spatial distribution of Hg in relation to visible alteration and the 0.34 ppm Au contour. Note the high detection limits for Hg (< 1 ppm Hg, plotted as 0.5 ppm) for the Placer Dome data in the surface holes, which limited understanding of the Hg halo above the HGB. B. Spatial distribution of Sb in relation of the 0.34 ppm Au contour and visible alteration. C. Spatial distribution of As in relation of the 0.34 ppm Au contour and visible alteration. Points represent individual analyses. Detailed discussion of patterns is in text.

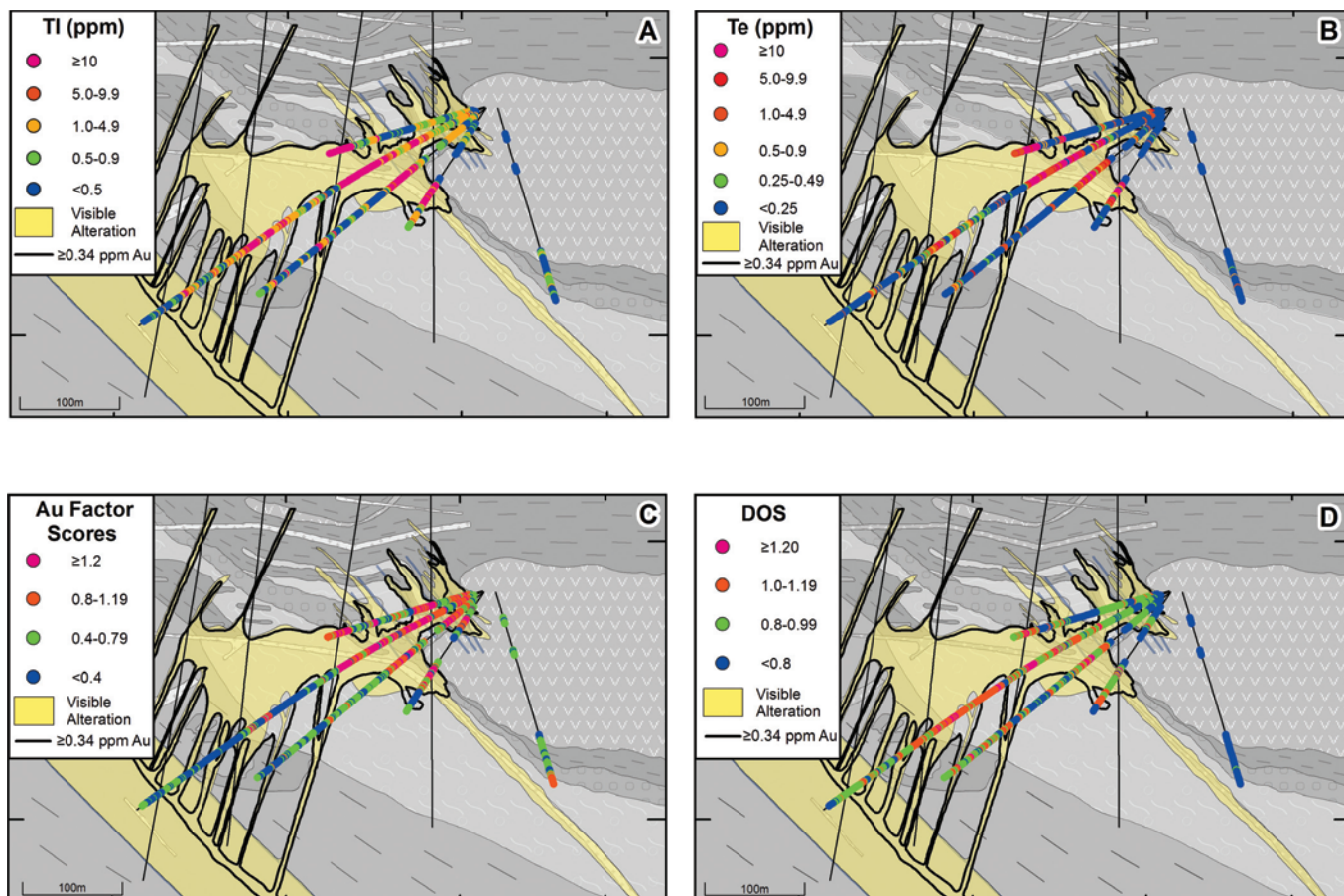


Figure 11. Spatial distribution of A. Tl, B. Te, C. Au-factor scores, and D. DOS, relative to visible alteration and the 0.34 ppm Au contour in the five underground holes. Points represent individual analyses and calculations. Detailed discussion of patterns is in text.

this ore-stage pyrite is potentially the only direct, visible indicator of ore in CTGDs. When abundant, hand samples containing this ore-stage pyrite have a sooty appearance under a hand lens. However, if not abundant, the ore-stage pyrite can be very difficult to recognize and differentiate from pre-ore pyrite. Though attempted, the presence and abundance of ore-stage sooty pyrite could not be consistently logged during this study, therefore, its distribution around the HGB ore zone is not understood.

Sulfidation has been argued to be the primary Au-deposition process associated with CTGDs, based on lithogeochemical data indicating S, rather than S and Fe, is added to the rock (Hofstra et al., 1991; Stenger et al., 1998). Loss of S from the hydrothermal fluid would destabilize aqueous gold-sulfide complexes in the hydrothermal fluid, resulting in gold deposition (Hofstra et al., 1991; Simon et al., 1999). Geochemical reaction path modeling has shown that sulfidation of host-rock iron can account for the gold content of pyrite and the ore grades observed in Carlin-type deposits (Hofstra et al., 1991). These geochemical models provide evidence that narrow high-grade ore zones result from host rocks containing higher initial reactive Fe contents (e.g., Fe within the carbonate crystal lattice).

Given the importance of ore-stage pyrite, the difficulty in systematically mapping its distribution, and the likelihood that it is the result of sulfur addition to the host rocks, we used the multi-element data from the five underground holes to calculate degree of sulfidation (DOS) to see whether it forms systematic patterns around the HGB.

$$\text{DOS} = \text{wt\% S} / [(1.15) (\text{wt\% Fe})] \quad (1)$$

The coefficient 1.15 is the Fe/S mass ratio in pyrite; thus, in the DOS notations, S contents are normalized to the amount of S necessary to convert all Fe in the rock to pyrite. Iron and S values from the five underground drill holes were analyzed utilizing a nitric aqua regia digestion followed by ICP-MS-AES. The ICP-MS-AES analyses were collected from 6m above and below zones of visible hydrothermal alteration, whereas Leco total S analyses were restricted to ore zones. Therefore, in order to verify the accuracy of the S analyses in both mineralized (≥ 0.1 ppm) and barren (< 0.01 ppm) samples, ICP-MS-AES samples were compared with Leco total sulfur analyses. Figure 12 shows excellent correlation between the Leco and ICP-MS-AES sulfur analyses, lending confidence in the reliability of the

Table 2. ANALYSES OF BACKGROUND SAMPLES.

Sample ID	Easting SP_NvW	Northing SP_NvW	Au ppb	Ag ppm	As ppm	Bi ppm	Ca %	Cu ppm	Fe %	Hg ppm	Mo ppm	Pb ppm	S wt%	Sb ppm	Se ppm	Sn ppm	Sr ppm	Te ppm	Tl ppm	W ppm	Zn ppm
GETBGLS1	856455	2355218	2.5	0.07	2.5	0.02	33.2	14.7	0.12	0.01	0.34	2.8	0.03	0.2	3	0.1	1380	0.03	0.08	0.4	53
GETBGLS2	857155	2363985	2.5	0.03	2.5	0.04	28.0	3.1	0.8	0.01	0.11	6.7	0.01	0.37	4	0.6	1020	0.14	0.1	0.5	24
GETBGLS3	855334	2364633	2.5	0.11	7	0.01	33.4	10	0.21	0.1	0.39	13.9	0.01	0.66	4	0.1	239	0.05	0.11	0.2	20
00NM164_1355	862223	2368222	2.5	0.11	2.5	0.23	17.3	30.8	2.8	0.01	0.27	7.1	0.43	1.1	3	1.6	889	0.06	0.4	1.5	74
00WM202_1839	862019	2360294	2.5	0.59	5	5.75	15.8	85.3	2.93	0.07	6.49	20.6	1.32	0.7	4	4.7	201	0.27	0.03	7.9	1860
00NM138_3384	870149	2366474	2.5	0.04	23	0.17	20.0	14.9	1.94	0.01	0.34	9.4	0.08	0.74	3	1.3	863	0.05	0.27	1.7	50
00NM138_5016.5	870124	2366231	2.5	0.15	14	0.25	10.8	56.9	6.61	0.01	1.63	19	0.66	1.15	3	2.2	102	0.03	0.54	1.3	129
00NM162A_2664.5	861522	2363804	2.5	0.07	2.5	0.16	26.7	14.8	1.84	0.01	0.67	1.8	0.51	0.12	4	0.4	418	0.12	0.1	0.5	36
00MW153_2748.5	875720	2368837	2.5	0.15	10	0.02	25.3	6.4	0.9	0.07	1.27	4.9	0.46	0.58	3	0.1	373	0.1	0.08	0.1	22
00MW161A_3753	877477	2368150	2.5	0.03	2.5	0.09	25.6	3	0.26	0.03	0.31	2.2	0.22	0.19	3	0.1	953	0.12	0.01	0.2	7
00MW140_3407.5	878380	2363408	2.5	0.01	2.5	0.13	18.9	14.3	2.04	0.01	0.16	7.3	0.05	0.11	2	1.2	665	0.08	0.35	0.6	45
00MW161A_3838	877476	2368143	2.5	0.05	6	0.01	23.4	2.8	0.55	0.03	0.35	2	0.13	0.25	3	0.1	881	0.06	0.02	0.2	4
GB4	848557	2289650	2.5	0.1	21	0.04	25.0	11	0.41	0.17	2.08	3.1	0.05	0.73	1.1	0.1	682	0.04	0.04	3.8	30
GB5	828917	2289722	7	0.08	11.0	0.01	25.0	2.10	0.25	0.07	1.38	1.10	0.02	0.18	0.90	0.10	903	0.03	0.01	1.89	17
Average			2.8	0.11	8	0.50	23.45	19.29	1.55	0.04	1.13	7.3	0.28	0.51	3	0.9	684	0.08	0.15	1.5	169

Coordinates are Nevada State Plane West, NAD27. Analyses are from samples collected from 8 core holes and 5 surface sites located at least 600 m from known mineralization. All of the drill core samples came from intervals that assayed <10 ppb Au for several tens of meters below and above. Analyses that were less than the detection limit for a given element were converted to half the detection limit.

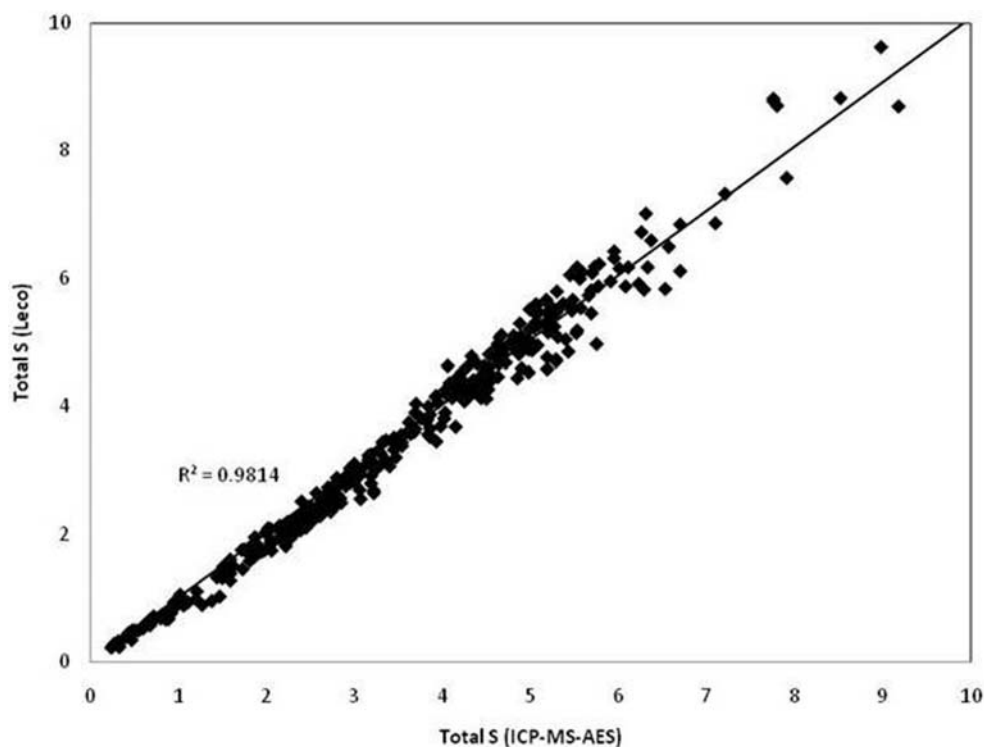


Figure 12. Plot of total wt% S determined by Leco versus wt% S determined by ICP-MS-AES. Note the strong positive correlation.

ICP-MS-AES S values. It is important to note that sulfates are uncommon at Turquoise Ridge and, therefore, the S values are reflecting sulfides. Though realgar is locally abundant in the five underground holes, pyrite is the predominant sulfide.

Figure 11D shows the spatial distribution of DOS values relative to the 0.34 ppm Au contour and zones of visible alteration. DOS values ≥ 0.8 show little to no halo beyond the 0.34 ppm Au contour and visibly altered wall rock in the upper parts of the HGB. Rather, pervasive ≥ 0.8 DOS values extend below the HGB in the zone of antithetic faults, with little to no change between visibly altered and unaltered rocks. DOS values of ≥ 1.2 are almost entirely restricted to zones of ≥ 3.4 ppm Au.

As was done by Stenger et al. (1998) for Twin Creeks, we plotted S values against the Fe values from the five underground holes to evaluate whether S and Fe or just S was introduced into the host rocks at Turquoise Ridge during mineralization (Figure 13). The line in Figure 13 marks the relative concentrations of S and Fe in pyrite [$S = 1.15 * \text{wt\% Fe}$]. The black arrows in Figure 13 represent trends in the data that would reflect either sulfidation or pyritization. Rocks undergoing sulfidation should show vertical trends toward the pyrite line. Complete sulfidation to form pyrite would occur at sulfur contents along the pyrite line for each individual sample. Rocks undergoing pyritization should show trends with a positive slope, indicating addition of both Fe and S. Data along the pyrite line indicates all the Fe in a given sample is now in the form of pyrite. Excess S in the samples above the pyrite line in Figure 13 is likely caused by other sulfides, such as orpiment and realgar. As seen in Figure

13, samples with < 0.01 ppm Au contain lower S, but not necessarily lower Fe, than samples with ≥ 3.4 ppm Au. This suggests sulfidation; however, we admit we are unable to know for certain if the ≥ 3.4 ppm Au samples contained similar initial Fe and S values as the < 0.34 ppm Au samples. Therefore, we cannot definitively distinguish between pyritization and sulfidation. The few samples with ≥ 3.4 ppm Au that contain > 4 wt% S and > 8 wt% Fe suggest pyritization, because there are no corresponding < 0.34 ppm Au samples with similar high Fe values, but with lower S values.

Decalcification

Dissolution and silicification of carbonate, as described above, is the most common alteration feature at the Turquoise Ridge deposit. Carbonate-bearing host rocks throughout the deposit contain abundant calcite, while pre-ore dolomite is only locally present in minor amounts. The zones of alteration shown on Figure 8A are where visible alteration could be correlated between drill holes. Though rocks outside the alteration zones on Figure 8A are mostly visibly unaltered, there are zones of visible alteration that are too narrow to correlate between holes. As has been noted, the multi-element data show that Ca negatively correlates with Au, which is to be expected if decalcification is the major alteration type associated with gold mineralization. Therefore, mapping the distribution of Ca might show increasing number of narrow alteration zones toward the larger zones of visible alteration shown in Figure 8A. Hence, point maps

were constructed from the five underground drill holes in order to compare the spatial distribution of Ca, Ca/Au, and Ca/Au factor score relative to visible alteration and the ≥ 0.34 ppm Au contour. Unfortunately, the distribution of Ca does not show an obvious halo of progressively decalcified rock beyond visible alteration and the >0.34 ppm Au contour. In general, Ca values $<0.5\%$ strongly correlate with ≥ 3.4 ppm Au throughout the HGB. Ca values are commonly $>10\%$ within meters of visible alteration. The distribution of Ca/Au and Ca/Au factor score also did not show any halo beyond visible alteration and the >0.34 ppm Au contour.

SPECTRAL REFLECTANCE DATA

Spectral reflectance data were collected using an Advanced Spectral Device (ASD) TerraSpec portable reflectance spectrometer to determine whether there were any patterns in clay mineralogy around the HGB ore zone. Minerals with the following radicals, molecules and bonds can be identified with spectral reflectance: OH^- , Al-OH^- , H_2O , SO_4^{2-} , CO_3^{2-} , Fe-OH^- , Mg-OH^- , and NH_4^+ . Therefore, the technique is most widely used to identify clay, sulfate, and carbonate minerals. Portable reflectance spectrometers such as the older PIMA and the newer ASD, are widely used in porphyry and epithermal systems to identify patterns in clay mineralogy around ore (cf. Thompson et al., 1999). Their use in CTGDs has been more limited, mainly because of the commonly dark, carbonaceous nature of the

rocks that host CTGDs. Dark rocks reflect very little light back into the spectrometer, resulting in spectra with low signal to noise ratios. Limited published spectral reflectance studies of CTGDs have reported ore associated with illite, kaolinite, and dickite (Hauff et al., 1991; Thompson et al., 1999)

In this study, we collected 1,065 spectra from the five underground holes and three of the surface holes in the cross-section. Spectra were collected from visibly unaltered wall rocks, variably altered rocks in zones with variable Au grades, and clay-lined fracture surfaces that were present in both visibly altered and unaltered wall rocks. The sampling focused on determining the clay mineral patterns around the 0.34 ppm Au contour. Spectra were individually interpreted visually by comparing unknown spectra with library spectra of known minerals using the software packages Specwin and Specmin, developed by Spectral International Inc. The minerals identified in this study included kaolinite, illite, muscovite, chlorite, montmorillonite, nontronite, beidellite, tremolite/actinolite, biotite, epidote, calcite, and dolomite. Samples containing spectra lacking interpretable mineralogical features or high background noise were excluded from the data set. Interpretable spectra were mainly limited to clay-lined fracture surfaces and light-colored rocks that included the upper, less carbonaceous limestone and brown mudstone, basalt, and dacite dikes. Very few interpretable spectra were collected from dark-colored rocks such as the lower carbonaceous mudstones and limestones and the sedimentary breccias. Therefore most of the in-

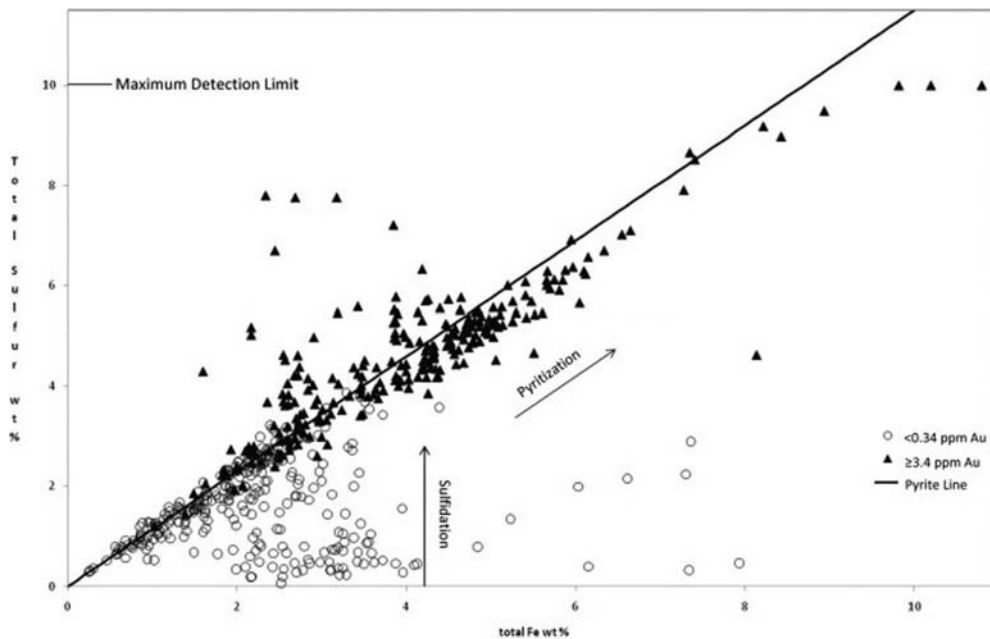


Figure 13. Plot of wt% S versus wt% Fe analyses from the five underground drill holes (derived from Stenger et al., 1998). Only drill intervals that contained limestone and had Au grades ≥ 3.4 ppm or <0.34 ppm are plotted. The line represents the ratio of S and Fe in pyrite. Samples that plot below the line indicate not all of the Fe in those samples has been sulfidized to form pyrite. Note that samples with grades between 0.34 and 3.4 ppm Au, which are not shown, would plot primarily on the pyrite line and significantly overlap with the samples with ≥ 3.4 ppm Au. Arrows depict the direction of compositional change related to sulfidation (vertical arrow) and pyritization (diagonal arrow).

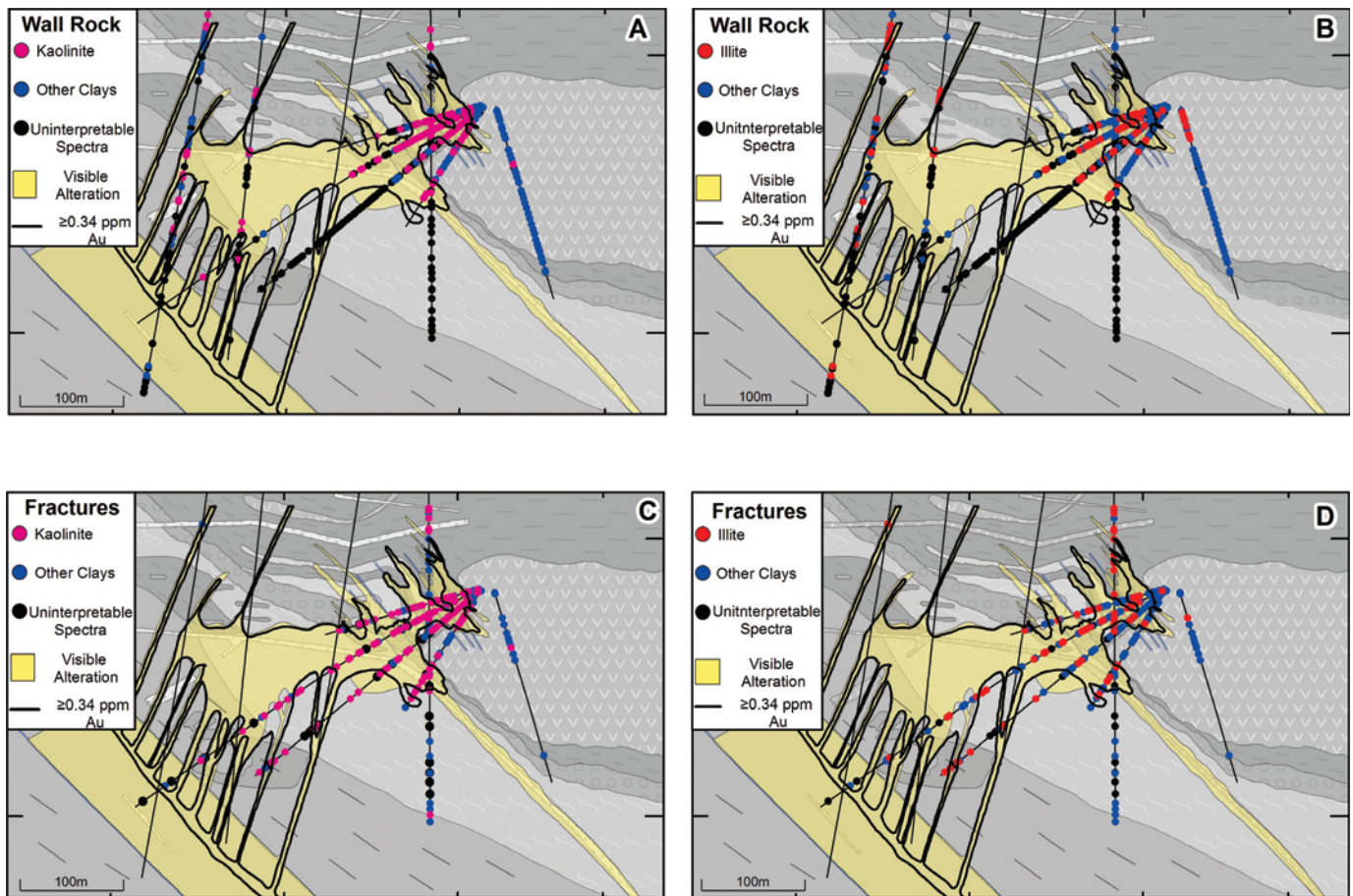


Figure 14. Results of spectral reflectance analyses showing spatial distribution of A. wall rock kaolinite, B. wall rock illite, C. kaolinite-bearing fracture surfaces, and D. illite-bearing fractures in relation to visible alteration and the 0.34 ppm Au contour.

terpretable data are in the upper parts of the cross-section (Figure 14). Ten representative samples from the dataset were analyzed by X-ray diffraction (XRD) to verify the ASD interpretations. The XRD results closely matched the ASD results.

Kaolinite was identified in 157 visibly altered wall rock samples and on 158 bleached fracture surfaces (Figure 14A,B). Many of the altered wall rock samples were from intervals within the HGB that had Au grades >3.4 ppm. The intimate spatial association between hydrothermal alteration, Au mineralization and kaolinite is strong evidence that kaolinite was coeval with ore formation as documented below. Beyond the 0.34 ppm Au contour, kaolinite-bearing rock samples occur along local, narrow zones of weak to moderate alteration. In addition, kaolinite-bearing fracture surfaces extend up to 4 m beyond visibly altered rock above the HGB, up to 20 m beyond visibly altered rock below the HGB, and for 15 m laterally beyond alteration zones associated with the antithetic faults.

Illite was detected in 94 visibly altered rock samples and on 79 fracture surfaces (Figure 14C,D). In visibly altered rock samples, illite displays a similar spatial distribution to kaolinite. Visibly altered rock samples containing illite primarily occur with Au grades >3.4 ppm within the HGB and rarely extend be-

yond the >0.34 ppm contour. Like kaolinite, illite-bearing fracture surfaces extend up to 4 meters beyond visibly altered rocks above the HGB, up to 20 meters below the HGB zone, and for 15 m laterally beyond alteration zones associated with the antithetic faults. We also recorded the sharpness of illite features and the wavelength of its main absorption feature, referred to here as the “2200 feature”. The wavelength of the 2200 feature in the illites ranged from 2198 nm to 2215 nm, with most between 2206 and 2208 nm. Illites with sharper features tended to have 2200 features with shorter wavelengths, mainly 2206 nm and below. However, neither the wavelength of the 2200 feature nor the sharpness of the illite features shows any systematic spatial relationship with respect to gold grade. In addition, no evidence for ammonium was seen in any of the illites.

Back scattered electron (BSE) imaging and energy dispersive spectroscopy (EDS) using a scanning electron microscope (SEM) were utilized to document the paragenetic relationships between ore minerals and kaolinite and illite. Kaolinite and/or illite were identified in multiple samples from zones containing >11 ppm Au. Kaolinite was identified with the SEM by high Al and Si peaks and a high Al/Si peak ratio using EDS. Illite was recognized by a significant K peak in addition to

Al and Si peaks. Under the SEM several ore-stage pyrite textures were recognized that are very similar to pyrite textures from Turquoise Ridge that were described by Longo et al. (2009). Arsenic peaks and, in some samples, Hg peaks were observed in these ore-stage pyrites, in addition to Fe and S peaks. Figure 15 shows examples of intimate intergrowths between ore-stage pyrite and either kaolinite or illite.

A Niton handheld XRF analyzer was used on a few visually unaltered samples with bleached, clay-lined fracture surfaces. The fracture surfaces and adjacent wall rock were analyzed. Calibration issues while conducting the XRF readings resulted in unreliable detection limits for most elements, with the exception of As. The results from four samples are shown in Table 3. In two samples, the As values are significantly

higher from kaolinite-lined fracture surfaces than from the adjacent wall rock, which suggests the clay-lined fractures represent limited flow of ore fluids in otherwise visibly unaltered rocks.

The remaining clay minerals identified with the ASD show no spatial association with Au, either within ore or as a halo to ore. Chlorite and nontronite occur in the NPB and adjacent tuffaceous mudstone in both the wall rock and along fracture surfaces. Montmorillonite is also commonly associated with the NPB and locally occurs in a few altered sedimentary rocks distal to the HGB, but shows no consistent pattern with respect to visible alteration or Au grades. Muscovite was identified in a few of the spectra and, based on thin section petrography, is most likely related to pre-ore metamorphism.

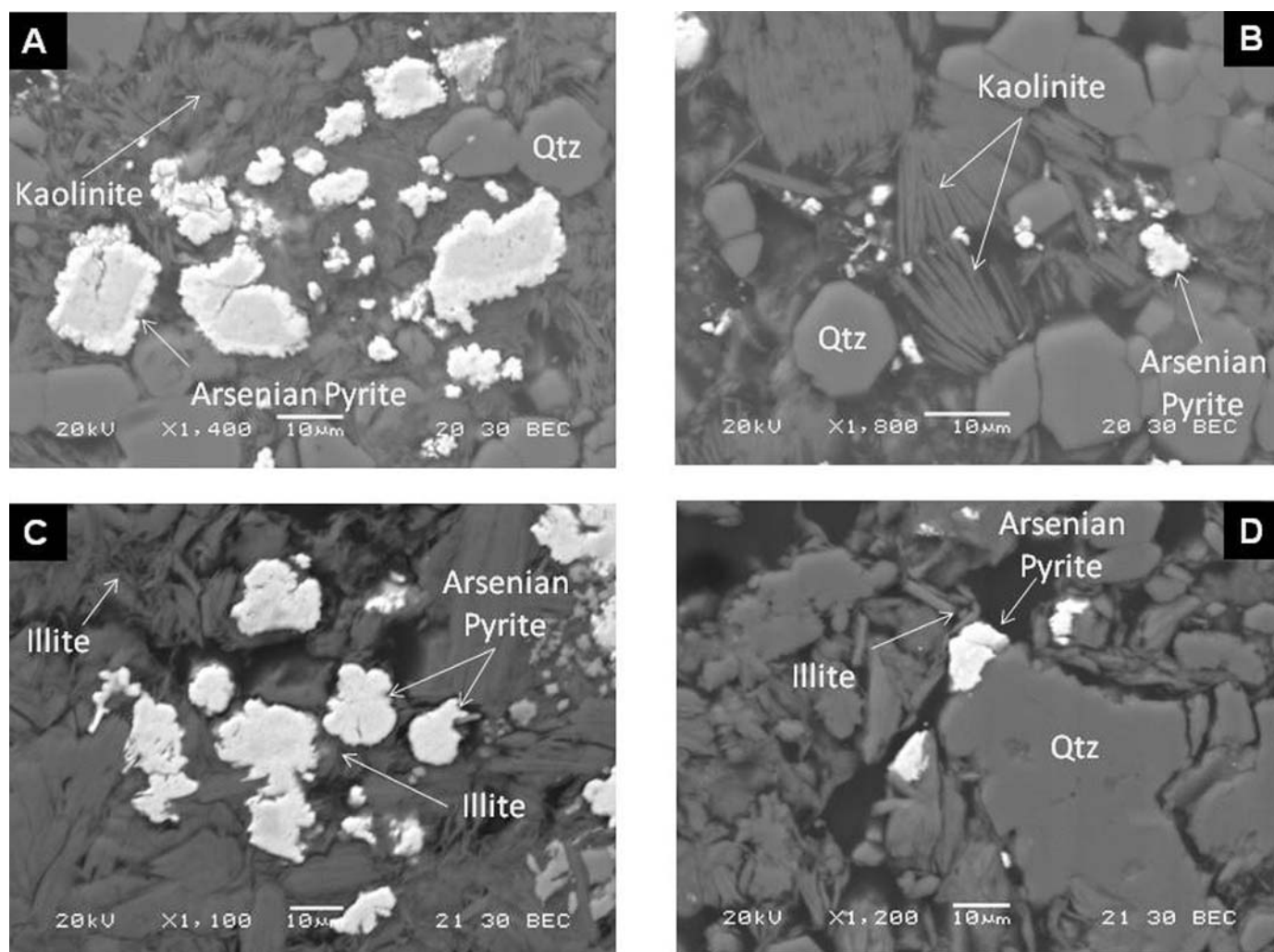


Figure 15. Back-scattered electron images of high-grade samples showing kaolinite and illite intergrown with ore-stage pyrite. A. Kaolinite intimately intergrown with ore-stage pyrite rimming a pre-ore pyrite grains in decalcified, silicified limestone. The rims contain As and Hg peaks using EDS, whereas the earlier pyrite cores showed no peaks with EDS other than Fe and S. B. Spheroidal pyrite containing ragged “fuzzy” edges with interstitial kaolinite and ore-stage quartz. C. Intimately intergrown ore-stage pyrite and illite. The large pyrite grain consists of a pre-ore pyrite core with no EDS peaks other than Fe and S. The edges of the core display dissolution textures and are rimmed by anhedral ore-stage pyrite. Also shown are spheroidal “fuzzy” pyrites. The illite occurs as radiating, sheet-like masses adjacent to the ore-stage pyrites. D. Intergrown illite and ore-stage pyrite adjacent to hydrothermal quartz in decalcified, silicified limestone.

Table 3. ASD AND NITON XRF RESULTS CONDUCTED ON ROCK AND FRACTURE SURFACES.

Drill Hole	DH Footage	Context	Rock type	Alteration	Au ppm Drill Interval	As ppm Niton	Kaolinite	Illite	2200 feature
TU01164A	454	Fracture Surface	Carbonaceous Black Mudstone	Bleached	0.017	83	X		2207?
TU01164A	454	Rock	Carbonaceous Black Mudstone	Unaltered	0.017	14	?	?	?
TU01166	613.5	Fracture Surface	Siliceous Black Mudstone	Bleached	0.01	1750	X	X	2207
TU01166	613.5	Rock	Siliceous Black Mudstone	Bleached	0.01	740	?	?	?
00NZ184	1828	Fracture Surface	Dacite	Unaltered	<0.01	< Deflection	X	X	2206
00NZ184	1828	Rock	Dacite	Unaltered	<0.01	< Deflection		X	2207
TU01164A	292	Fracture Surface	Brown Mudstone	Bleached	0.045	57		X	2199
TU01164A	292	Rock	Brown Mudstone	Unaltered	0.045	61	?	?	?

? – spectrum was too noisy to interpret or adjacent rock was not analyzed with the ASD

DISCUSSION

This study set out to define the nature and extent of the hydrothermal features around a high-grade ore zone in an underground Carlin-type deposit, with the goal of deriving practical tools that might aid in mine development and the discovery of future ore zones at Turquoise Ridge and other CTGDs. Table 4 summarizes the data sets presented in this study, whether or not they formed haloes, and the size of the haloes. The most coherent haloes to the HGB ore zone at Turquoise Ridge are Au values ≥ 0.34 ppm and visible hydrothermal alteration in the form of decalcification, argillization and silicification. Similar to what was reported by Muntean et al. (2009), moderate to strong alteration closely correlates spatially with gold grades ≥ 0.34 ppm. Lower Au grades extend beyond the 0.34 ppm contour but are not sufficiently persistent to be contoured.

Statistical analysis of multi-element data in this study shows Au is associated mainly with Hg, As, W, S, Tl, Sb, and Te. With the exception of As and possibly Hg, the spatial distribution of trace elements related to Au do not form large, coherent haloes to Au that would effectively serve exploration or development. Arsenic values of ≥ 100 ppm can be contoured and extend up to 30 m

beyond visible alteration and the 0.34 ppm Au contour. The greater dispersion of As relative to the other ore-related elements might be partly caused by the presence of arsenic sulfides. However, the 100 ppm As contour commonly extends into areas without visible realgar or orpiment. Other sulfides, such as cinnabar and stibnite are rare at Turquoise Ridge; therefore, most of the ore-related elements are likely in the ore-stage pyrite. The extent of anomalous Hg levels above the HGB, in the range of 0.04 to 1 ppm, is unknown because of the high detection limits for the analyses from the four surface holes. Given the lack of haloes in other ore-related trace elements, it should be no surprise that factor scores for the gold factor (Factor 2 in Table 1) did not show any consistent halo around visible alteration and the 0.34 ppm Au contour. Moreover, the lack of haloes in DOS values suggest the amount of ore-stage pyrite probably decreases away from ore in the same manner as does Au and the ore-related elements (except As and possibly Hg). This suggests there is not a large halo of ore-stage pyrite that is poor in trace elements surrounding the zones of visible alteration at Turquoise Ridge. Another possible explanation for the lack of a recognizable halo in DOS values could be variations in the amount of pre-ore pyrite and/or the amount of Fe in the various lithologies at Turquoise Ridge.

Table 4. SUMMARY OF THE EXTENT OF HALOES OF FEATURES AT TURQUOISE RIDGE.

Feature	Occurs within >0.34 ppm Au contour and visible alteration	Forms halo to >0.34 ppm Au contour and visible alteration	Maximum extent of halo (meters)	Nature of Halo
As (≥ 100 ppm)	Yes	Yes	30	coherent halo
Sb (≥ 5 ppm)	Yes	Yes	12	coherent halo
Hg (≥ 1 ppm)	Yes, coincident	No	–	–
Tl (≥ 5 ppm)	Yes, smaller	No	–	–
Te (≥ 1 ppm)	Yes, smaller	No	–	–
Au Factor Scores (≥ 0.8)	Yes, smaller	No		locally occurs outside of visible alteration but forms no pattern
DOS (≥ 0.8)	Yes, coincident	Yes	<5	local, discontinuous halo below HGBC
Ca (>5 wt%)	Yes	No	–	rarely occurs outside of visible alteration
Kaolinite-coated fracture surfaces	Yes	Yes	20	discontinuous halo
Illite-coated fracture surfaces	Yes	Yes	20	discontinuous halo
RQD (<25%)	Yes	Yes	30	coherent halo

Gold negatively correlates with Mg, Ca, and Sr, which directly reflects the dissolution of carbonate during ore formation; therefore, it is tempting to map decalcification by plotting Ca values. However, when Ca, Ca/Au and Ca/Au factor scores were plotted, they displayed no obvious halo relative to visible alteration. The inability of Ca values to track very weak alteration or narrow zones of stronger alteration surrounding ore is probably because the variation in the Ca content of the various lithologies at Turquoise Ridge is greater than the variation in Ca caused by such weak or narrow zones of decalcification.

The ASD analyses and SEM work demonstrate kaolinite and illite are spatially and temporally associated with Au mineralization and the ore-stage pyrite. Kaolinite and illite are the dominant clay minerals found within moderate to strong alteration zones containing ≥ 3.4 ppm Au. Fractures surfaces containing kaolinite and/or illite extend up to 20 m beyond the 0.34 ppm Au contour. Furthermore, the limited data collected with the Niton handheld XRF suggest these clay-lined fractures contain strongly anomalous As and possibly other trace elements.

Few maps and cross-sections depicting haloes of low-grade Au, alteration, and trace elements around CTGDs are available in the literature. Table 5 is a non-exhaustive compilation of published data. Only examples, where two or three-dimensional data were reported are included, whereas publications that only had one-dimensional data (e.g. transects, individual drill holes) were not included. Examples of both high-grade underground deposits, similar to Turquoise Ridge, and lower-grade open pit deposits are listed. High-grade underground deposits, like the Deep Star deposit in the northern Carlin trend, show abrupt patterns in gold grade similar to Turquoise Ridge. At Deep Star, Au values of ≥ 0.34 ppm extend only 0-30 m beyond the 6.8 ppm Au contour (Heitt et al., 2003). The lower-grade underground deposits and especially the large open pit deposits have low gold grades that extend for much further distances beyond ore than they do at Turquoise Ridge. For example, the 0.34 ppm Au contour extends for 100-300 m beyond the 6.8 ppm Au contour at the Twin Creeks (Megapit), Gold Quarry, Leeville, and Turf deposits. However, like Turquoise Ridge, visible alteration zones at Twin Creeks and Gold Quarry roughly coincide with the 0.34 ppm Au contour. The data from the underground Ren deposit suggests very low grades of Au (≥ 0.020 ppm) can form large, albeit inconsistent, haloes several hundred meters above ore, but not below ore. The open pits with low-grade ore that were mined at Turquoise Ridge prior to underground mining are likely an example of such a halo, although the patterns of gold grades between the open pit and the underlying individual ore zones, like the HGB, have not been established in detail. Though difficult to directly compare, the limited trace element data summarized in Table 5 suggest patterns not dissimilar to Turquoise Ridge.

Like Turquoise Ridge, kaolinite has been identified in a number of CTGDs, of which some also have dickite (e.g., Alligator Ridge, 1990, Ilchick; Vista ore-body at Twin Creeks, Osterberg and Guilbert, 1991; Carlin, Kuehn and Rose, 1992; Betze Post, Arehart et al., 1993b; Deep Star, Heitt et al., 2003).

In most cases, like at Turquoise Ridge, the zone of kaolinite-bearing alteration is restricted to ore zones. For example, kaolinite-bearing alteration at Deep Star is restricted to Au grades of ≥ 6.8 ppm. Similar to Turquoise Ridge, kaolinite-bearing veinlets extend beyond ore for several tens of meters at Alligator Ridge (Ilchik, 1990), Carlin (Kuehn and Rose, 1992), and Screamer (Ye et al., 2003) CTGDs.

The lack of wide, coherent haloes of various hydrothermal features surrounding ore at Turquoise Ridge is suggestive of a restrictive, fracture-controlled fluid flow network, rather than large-scale, pervasive, lithologic-controlled fluid flow. As pointed out by Muntean et al. (2009), ore fluids likely ascended along the pre-existing Getchell fault zone and into the steep, small-displacement, antithetic faults in the hanging wall as well as the main dacite porphyry dike before encountering highly-fractured, reactive carbonate lithologies, especially the sedimentary breccias and the deformed mudstones and limestones adjacent to edge of the NPB. Increased surface area in these fractured zones allowed more fluid:rock interaction, which resulted in more extensive carbonate dissolution, sulfidation, and Au mineralization in the HGB. The exploitation of these pre-existing fracture networks by the hydrothermal fluids is supported by the large zone of RQD values that are $< 25\%$, which probably forms a better halo to visible alteration and ≥ 0.34 ppm Au than any of the hydrothermal features presented in this paper.

RECOMMENDATIONS

The results of this study demonstrate that the most reliable tools to use for vectoring into ore at Turquoise Ridge, and likely other high-grade ore zones in and around other CTGDs, is carefully hand-contouring gold grades and visible alteration on cross-sections. Carefully logged decalcification, dedolomitization, argillization, and possibly silicification should be lumped together when contouring alteration. The contouring needs to be done after geology is carefully logged, plotted and interpreted on cross-sections, ideally by the same geologist. The cross-section work should then be followed by three-dimensional modeling of various gold grade shells and surfaces of visible alteration. We realize that cross-section work can be viewed as obsolete, given the complex three-dimensional geometry of CTGDs and the wide availability of sophisticated modeling software. However, until it can be demonstrated that detailed logging information (e.g., multiple lithologies, complex structures, etc.) can be effectively and routinely incorporated into the interpretation of three-dimensional surfaces of gold grades and alteration, we are convinced that detailed cross-section work should be included in the development of three-dimensional models for CTGDs.

With the exception of As and Sb, and possibly Hg, this study showed that other ore-related elements did not form coherent haloes around visible alteration associated with the HGB at Turquoise Ridge. The apparent tightly-confined nature of fluid flow throughout the Turquoise Ridge deposit appears to

Table 5. CHARACTERISTICS OF HYDROTHERMAL HALOS SURROUNDING ORE IN OTHER CTGDS.

Deposit	Nature of halos around ore	References
Twin Creeks (Megapit)	<ol style="list-style-type: none"> 1. The 0.34 ppm Au contour extends up to 150 m beyond the 1.7 ppm Au contour. 2. The 100 ppm As contour extends up to 90 m beyond the 1.7 ppm Au contour. 3. The 50 ppm Sb contour extends up to 70 m beyond the 1.7 ppm Au contour. 4. The 10 ppm Hg contour extends up to 90 m beyond the 1.7 ppm Au contour. 5. The As, Sb, and Hg contours mentioned above do not appear to form haloes around the 0.34 ppm Au contour. 6. The <5 wt% total carbonate contour extends up to 40 m beyond the 1.7 ppm Au contour. 	1. Stenger et al., 1998
Deep Star (underground)	<ol style="list-style-type: none"> 1. The 0.34 ppm Au contour extends 0 to 30 m beyond the 6.8 ppm Au contour. 2. Kaolinite-bearing wall rock alteration occurs within the 6.8 ppm Au contour. 3. The 100 ppm As contour extends at least 400 m above the 6.8 ppm Au contour. 	1. Heitt et al., 2003
Alligator Ridge (Vantage pit)	<ol style="list-style-type: none"> 1. Au grades commonly decrease from >3 ppm to <0.1 ppm over distances of <5 m. 2. Zone of decarbonatization coincides with the ore-waste boundary. 3. Kaolinite-bearing veinlets extend 75 m beyond ore. 	1. Ilchik, 1990
Carlin	<ol style="list-style-type: none"> 1. Decalcification extends 25 m above and 75 m below the 1 ppm Au contour 	1. Kuehn and Rose, 1992
Ren	<ol style="list-style-type: none"> 1. Au grades of 0.02 ppm form a discontinuous halo 350 m above the 1 ppm Au contour, but do not form a halo below the 1 ppm Au contour. 2. The 25 ppm As contour extends up to 60 m beyond the 1 ppm Au contour. 3. The 2 ppm Sb contour extends up to 120 m beyond the 1 ppm Au contour. 4. The 0.5 ppm Hg contour extends up to 70 m above the 1 ppm Au contour, but only m below the 1 ppm Au contour. 	1. Albino, 1994
Gold Bar	<ol style="list-style-type: none"> 1. The 0.034 ppm Au contour extends 50 m above ore, but not below ore. 2. Weak decalcification forms a zone that is slightly larger than the 0.068 ppm Au contour. 3. The 100 ppm As contour is mostly coincident with ore. 4. The 20 ppm Sb contour is mostly coincident with ore. 5. The 1 ppm Hg contour forms a halo to ore. 	<ol style="list-style-type: none"> 1. Broili et al., 1988 2. Masinter, 1990
Turf	<ol style="list-style-type: none"> 1. Decalcification extends up to 100 m beyond the 6.8 ppm Au contour. 	1. Mohling, 2002
Leeville	<ol style="list-style-type: none"> 1. Decalcification extends up to 120 m beyond the 6.8 ppm Au contour. 	1. Jackson et al., 2002
Gold Quarry	<ol style="list-style-type: none"> 1. The 0.34 ppm Au contour extends up to 200 to 300 m from zones of ≥ 6.8 ppm Au. 2. The zone of fairly continuous alteration is roughly coincident to slightly smaller than the 0.34 ppm Au contour. 	1. Harlan et al., 2002

have prevented the development of large-scale pervasive dispersion haloes around the HGB. This is likely the case in many CTGDs. Although trace elements provide critical information in the early stages of exploration by helping determine if mineralization has an elemental signature consistent with known CTGDs (e.g., Au-As-Hg-Tl-Sb with low Cu-Pb-Zn-Ag), they might not provide haloes that are any larger or more coherent than Au itself. When core holes are drilled, RQD values should be determined and contoured.

Besides simply contouring gold grades and visible alteration, another promising vectoring tool that might very well detect large, but likely inconsistent, haloes to contourable gold grades and visible alteration in otherwise unaltered rock is the analysis of fracture surfaces. This study demonstrated kaolinite- and illite-bearing fractures surfaces, as determined by reflectance spectroscopy, extended up to 20 m beyond contourable gold and alteration. Though these haloes are still somewhat narrow, such analyses should be done over a larger volume of rock at Turquoise Ridge and other CTGDs to see if

haloes are larger and if the approach is indeed viable. More importantly, determination of the clay mineralogy along such fracture surfaces might be unnecessary, if such fracture surfaces are demonstrated to contain anomalous As-Hg-Tl-Sb by using a portable Niton XRF. Limited use of the Niton in this study suggested the kaolinite- and illite-bearing fractures surfaces might contain more As than adjacent unaltered wall rock. More mining and exploration companies are using such portable XRF units, but few to no data have been published. Comprehensive orientation studies of CTGDs are warranted.

ACKNOWLEDGEMENTS

The authors would like to thank the Barrick Gold Corp. and the Turquoise Ridge staff, especially Karl Marlowe, Keith Wood, and John Carlson for permitting publication of this paper and allowing complete access to Turquoise Ridge, including drill core and all available data. This paper constitutes a portion of MC's Master's thesis research at the University of Nevada

Reno. The authors would like to thank Greg Arehart and an unnamed editor for thoughtful reviews of the manuscript. Funding for this project was provided by the National Science Foundation (EAR award 0635657), the USGS MERIT program, Barrick Gold Corp., and Placer Dome Exploration Inc. JM would like to acknowledge all of the current and past Turquoise Ridge geologists, especially his former colleagues at Placer Dome, who are responsible for developing the extensive database and much of the geologic framework at Turquoise Ridge.

REFERENCES

- Abdi, H., 2003, Factor Rotations in Factor Analyses, in Lewis-Beck M., Bryman, A., and Futing, T., eds., *Encyclopedia of Social Sciences Research Methods*, Thousand Oaks, CA: Sage, p. 1–8.
- Albino, G.V., 1994, Geology and lithochemistry of the Ren gold prospect, Elko County, Nevada: the role of rock sampling in exploration for deep Carlin-type deposits: *Journal of Geochemical Exploration*, v. 51 p. 37–58.
- Arehart, G.B., Chryssoulis, S.L., and Kesler, S.E., 1993a, Gold and arsenic in iron sulfides from sediment-hosted disseminated gold deposits: Implications for depositional processes: *Economic Geology*, v. 88, p. 171–185.
- Arehart, G.B., Foland, K.A., Naeser, C.W., and Kesler, S.E., 1993b, $^{40}\text{Ar}/^{39}\text{Ar}$, K/Ar, and fission track geochronology of sediment-hosted disseminated gold deposits at Post-Betze, Carlin trend, northeastern Nevada: *Economic Geology*, v. 88, p. 622–646.
- Arehart, G.B., Chakurian, A.M., Tretbar, D.R., Christensen, J.N., McInnes, B.A., and Donelick, R.A., 2003, Evaluation of radioisotope dating of Carlin-type deposits in the Great Basin, North America, and implication for deposit genesis: *Economic Geology*, v. 98, p.235–248.
- Bakken, B.M., and Einaudi, M.T., 1986, Spatial and temporal relations between wall rock alteration and gold mineralization, main pit, Carlin gold mine, Nevada, USA, in *Proceedings, Gold '86; an international symposium on the geology of gold deposits*, Toronto, ON, Canada, p. 388–403.
- Berger, B.R., and Taylor, B.E., 1980, Pre-Cenozoic normal faulting in the Osgood Mountains, Humboldt County, Nevada: *Geology*, v. 8, p. 594–598.
- Boskie, R.M., 2001, Detailed structure and stratigraphy of the lower Paleozoic rocks of the Getchell trend, Osgood Mountains, Humboldt County, Nevada: unpublished Masters thesis, University of Nevada Reno, 171 p.
- Breit, F.J., Ressel, M.W., and Muirhead, E.M.M., 2005, Geology and gold deposits of the Twin Creeks Mine, Humboldt County, Nevada, in *Sediment-Hosted Gold Deposits of the Getchell District, Nevada Geological Society of Nevada Symposium 2005, Field Trip Guidebook 4*, p. 77–102.
- Broili, C., French, G.M., Shaddrick, D.R., Weaver, R.R., 1988, Geology and gold mineralization of the Gold Bar deposit, Eureka County, Nevada, in Schaefer, R.W., Cooper, J.J., and Vikre, P.G., eds., *Bulk mineable precious metal deposits of the Western United States: Geological Society of Nevada*, p. 57–72.
- Buchanan, L.J., 1981, Precious metal deposits associated with volcanic environments in the southwest: *Arizona Geological Society Digest*, v. 14, p. 237–262.
- Chevillon, V., Berentsen, E., Gingrich, M., Howald, B., Zbinden, E., 2000, Geologic overview of the Getchell gold mine geology, exploration, and ore deposits, Humboldt County, Nevada, in Crafford, E.J., ed., *Geology and gold deposits of the Getchell region, Guidebook Series Society of Economic Geologists*, v. 32, p. 195–201
- Cline, J.S., 2001, Timing of gold and arsenic sulfide mineral deposition at the Getchell Carlin-type gold deposit, North-central Nevada: *Economic Geology*, v. 96, p. 75–90.
- Cline, J.S., Hofstra, A.H., Muntean, J.L., Tosdal, R.M., and Hickey, K.A., 2005, Carlin-type gold deposits in Nevada: Critical geologic characteristics and viable Models: in Hedenquist, J. W., Thompson, J. F. H., Goldfarb, R. J., and Richards, J. P., eds., *100th Anniversary Volume: Society of Economic Geologists*, Littleton, CO, p. 451–484.
- Cline, J.S., Muntean, J. L., Longo, A.A., and Cassinero, M.D., 2008, Collaborative research on fluid pathway and metal transport in Carlin-type gold deposits: Insights from the Getchell deposit. Final Report for the U.S. Geological Survey 2006 Mineral Resources External Research Program (MRERP), 128 p.
- Crafford, E.J., 2000, Overview of regional geology and tectonic setting of the Osgood Mountains region, Humboldt County, Nevada, in Crafford, E.J., ed., *Geology and gold deposits of the Getchell region, Guidebook Series Society of Economic Geologists*, v. 32, p. 225–234.
- Cook, H.E. and Taylor, M.E., 1977, Comparison of continental slope and shelf environments in the Upper Cambrian and lowest Ordovician of Nevada: in Cook, H. E. and Enos, P., eds. *Deep-water carbonate environments: SEPM Special Publication 25*, p. 51–81.
- Dong, G, Morrison, G., and Jaireth, S., 1995, Quartz textures in epithermal veins, Queensland—classification, origin, and implication: *Economic Geology*, v. 90, p. 1841–1856.
- Emsbo, P., Hutchinson, R.W., Hofstra, A.H., Volk, J.A., Bettles, K.H., Baschuk, G.J., and Johnson, C.A., 1999, Syngenetic Au on the Carlin trend: Implications for Carlin-type deposits: *Geology*, v. 27, p. 59–62.
- Groff, J.A., Heizler, M.T., McIntosh, W.C., Norman, D.I., 1997, $^{40}\text{Ar}/^{39}\text{Ar}$ dating and mineral paragenesis for Carlin-type gold deposits along the Getchell Trend, Nevada; evidence for Cretaceous and Tertiary gold mineralization: *Economic Geology*, v. 92, p. 601–622.
- Gustafson, L.B. and Hunt, J.P., 1975, The porphyry copper deposit at El Salvador, Chile: *Economic Geology* v. 70, p. 857–912.
- Harlan, J.B., Harris, D.A., Mallette, P.M., Norby, J.W., Rota, J.C., and Sagar, J.J., 2002, Geology and mineralization of the Maggie Creek district: in Thompson, T.B., Teal, L., and Meeuwig, R.O., eds., *Gold Deposits of the Carlin Trend: Nevada Bureau of Mines and Geology Bulletin 111*, p. 115–142.
- Hauff, P.L., Kruse, F.E., Madrid, R.J., 1991, Defining gold ore zones using illite polytypes, in Raines, G.L., Lisle, R.E., Schafer, R.W., Wilkinson, W.H., eds., *Geology and Ore Deposits of the Great Basin Symposium Proceedings*, Geological Society of Nevada, p. 239–247.
- Hall, C.M., Kesler, S.E., Simon, G., Fortuna, J., 2000, Overlapping Cretaceous and Eocene Alteration, Twin Creeks Carlin-type deposit, Nevada: *Economic Geology*, v. 95, no. 8, p. 1739–1752.
- Hedenquist, J.W., Arribas R., A., and Gonzales-Urien, E., 2000, Exploration for epithermal gold deposits, in Hagemann, S.G., and Brown, P.E., eds., *Gold in 2000: Reviews in Economic Geology*, v. 13, p. 245–277.
- Heitt, D.G., Dunbar, W.W. Thompson, T.B., and Jackson, R.G., 2003, Geology and geochemistry of the Deep Star gold deposit, Carlin trend, Nevada: *Economic Geology*, v. 98 p. 1107–1136.
- Hofstra, A.H., 1994, Geology and genesis of the Carlin-type gold deposits in Jerritt Canyon district, Nevada: unpublished Ph.D. thesis, Boulder, University of Colorado, 791 p.
- Hofstra, A.H., and Cline, J.S., 2000, Characteristics and models for Carlin-type gold deposits: in Hagemann, S.G., and Brown, P.E., eds., *Gold in 2000: Reviews in Economic Geology*, v. 13, p. 163–220.
- Hofstra, A.H., Leventhal, J.S., Northrop, H.R., Landis, G.P., Rye, R.O., Birak, D.J., and Dahl, A.R., 1991, Genesis of sediment-hosted disseminated gold deposits by fluid mixing and sulfidization: Chemical-reaction-path modeling of ore-depositional processes documented in the Jerritt Canyon District, Nevada: *Geology*, v. 19, p.36–40.
- Hofstra, A.H., Snee, L.W., Naeser, C.W., Stein, H.J., and Lewchuck, M., 1999, Age constraints on Jerritt Canyon and other Carlin-type gold deposits in the western United States—relationship to mid-Tertiary extension and magmatism: *Economic Geology*, v. 94, p. 769–802.

- Horton, R. C., 1999, History of the Getchell gold mine: Mining Engineering, v. 51, p. 50–56.
- Hotz, P.E., and Willden, R., 1964, Geology and mineral deposits of the Osgood Mountains quadrangle, Humboldt County, Nevada: U.S. Geological Survey Professional Paper 431, 128 p.
- Ilchick, R.P., 1990, Geology and geochemistry of the Vantage gold deposits, Alligator Ridge-Bald Mountain mining district, Nevada: Economic Geology, v. 85, p. 50–75.
- Jackson, M., Lane, M., Leach, B., 2002, Geology of the West Leeville Deposit: in Thompson, T.B., Teal, L., and Meeuwig, R.O., eds., Gold Deposits of the Carlin Trend: Nevada Bureau of Mines and Geology Bulletin 111, p.106–114.
- Joraleman, P., 1951, The occurrence of gold at the Getchell mine, Nevada, Economic Geology, v. 46, p. 276–310.
- Kuehn, C.A., and Rose, A.R., 1992, Geology and geochemistry of wall-rock alteration at the Carlin gold deposit, Nevada: Economic Geology, v. 87, p. 1697–1721.
- Lowell, J.D., and Guilbert, J.M., 1970, Lateral and vertical alteration-mineralization zoning in porphyry ore deposits: Economic Geology, v. 65, p. 373–408.
- Longo, A.A., Cline, J.S., and Muntean, J.L., 2009, Using pyrite to track evolving fluid pathways and chemistry in Carlin-type deposits: Diverse Gold Deposits of the Osgood Mountains and Humboldt Range, North-Central, Nevada, Geological Society of Nevada Special Publication no. 49, p.63–65.
- Lovering, T.G., 1972, Jasperoid in the United States—its characteristics, origin, and economic significance: U.S Geological Survey Professional Paper 710, 164 p.
- Madden-McGuire, D.J., and Marsh, S.P., 1991, Lower Paleozoic host rocks in the Getchell gold belt; several distinct allochthons or a sequence of continuous sedimentation?: Geology, v. 19, p. 489–492.
- Madrid, R. J. J., 1987, Stratigraphy of the Roberts Mountains allochthon in north-central Nevada: unpublished PhD thesis, Stanford University, 341 p.
- Masinter, R.A., 1990, Geology, wall-rock alteration, and gold mineralization of the Gold Bar deposit, Eureka County, Nevada, unpublished Masters thesis, Stanford University, 256 p.
- Marlowe, K., Wood, K. and Muntean, J., 2007, The Getchell mine complex: Seven decades of mining and geology: in Johnston, M. K. ed., Faults, Folds, and Mineral Belts: Regional Structural Systems, Gold Mineralization, and Exploration Potential in the Great Basin, Geological Society of Nevada Special Publication No. 46, p. 127–134.
- McLachlan, C.D., Struhsacker, E.M., and Thompson, W.F., 2000, The gold deposits of Pinson Mining Company; a review of the geology and mining history through 1999, Humboldt County, Nevada: in Crafford, E.J. ed., Geology and gold deposits of the Getchell region, Guidebook Series Society of Economic Geologists, v. 32, p. 207–223.
- Mohling, J.W., 2002, Geology and gold mineralization of the Turf Deposit: Geology and mineralization of the Maggie Creek district: in Thompson, T.B., Teal, L., and Meeuwig, R.O., eds., Gold Deposits of the Carlin Trend: Nevada Bureau of Mines and Geology Bulletin 111, p.91–105.
- Muntean, J. L., Coward, M. P., and Tarnocai, C. A., 2007, Reactivated Palaeozoic normal faults: controls on the formation of Carlin-type gold deposits in north-central Nevada: in Reis, A. C., Butler, R. W. H. and Graham, R. H., eds., Deformation of the Continental Crust—The Legacy of Mike Coward: Geological Society, London, Special Publications, v. 272, p. 573–589.
- Muntean, J.L., Cassinero, M.D., Arehart, G.B., Cline, J.S., and Longo, A.A., 2009, Fluid pathways at the Turquoise Ridge Carlin-type gold deposit, Getchell district, Nevada: Diverse Gold Deposits of the Osgood Mountains and Humboldt Range, North-Central, Nevada, Geological Society of Nevada Special Publication no. 49, p. 67–69.
- Nevada Bureau of Mines and Geology, 2009, The Nevada Mineral Industry 2008: Special Publication MI-2008, p. 175.
- Osterberg, M.W., and Guilbert, J.M., 1991, Geology, wall-rock alteration, and new exploration techniques at the Chimney Creek sediment-hosted gold deposit, Humboldt County, Nevada, in Raines, G.L., Lisle, R.E., Schaefer, R.W., and Wilkinson, W.H., eds., Geology and Ore Deposits of the Great Basin Symposium Proceedings, Geological Society of Nevada, p. 805–821.
- Patterson, L.M., 2009, Hydrothermal footprint of Carlin-type gold deposits at the district scale: Jerritt Canyon mining district, Elko County, Nevada: unpublished Masters thesis, University of Nevada, Reno, 240 p.
- Reich, M., Kesler, S.E., Utsunoyiya, S., Palenik, C.S., Chryssoulis, S., and Ewing, R.C., 2005, Solubility of gold in arsenian pyrite: *Geochemica et Cosmochimica Acta*, vol. 69, p. 2781–2796.
- Seedorff, E., Dilles, J.H., Proffett, J.M., Einaudi, M.T., Zurcher, L., Stavast, W.J.A., Johnson, D.A., and Barton, M.D., 2005, Porphyry deposits: characteristics and origin of hypogene features: in Hedenquist, J.W., Thompson, J.F.H., Goldfarb, R.J., and Richards, J.P., eds., 100th Anniversary Volume: Society of Economic Geologists, Littleton, CO, p. 251–298.
- Sha, P., 1993, Geochemistry and genesis of sediment-hosted disseminated gold mineralization at the Gold Quarry mine, Nevada: unpublished Ph.D. thesis, University of Alabama, 228 p.
- Simmons, S.F., White, N.C., and John, D.A., 2005, Geological characteristics of epithermal precious and base metal deposits: in Hedenquist, J.W., Thompson, J.F.H., Goldfarb, R.J., and Richards, J.P., eds., 100th Anniversary Volume: Society of Economic Geologists, Littleton, CO, p. 451–484.
- Simon, G., Kesler, S.E., and Chryssoulis, S., 1999, Geochemistry and textures of gold bearing arsenian pyrite, Twin Creeks, Nevada: Implications for deposition of gold in Carlin-type deposits: Economic Geology, v. 94, p. 405–422.
- Stenger, D.P., Kesler, S.E., Peltonen, D.R., and Tapper, C.J., 1998, Deposition of gold in Carlin-type deposits; the role of sulfidation and decarbonation at Twin Creeks, Nevada: Economic Geology v. 93, p. 201–215.
- Thompson, A.J.B., Hauff, P.L., and Robitaille, A.J., 1999, Alteration mapping in exploration: Application of short-wave infrared (SWIR) spectroscopy: SEG Newsletter, no. 39, p. 1, 16–28.
- Tretbar, D., Arehart, G.B., and Christensen, J.N., 2000, Dating gold deposition in a Carlin-type gold deposit using Rb/Sr methods on the mineral galkhaite: Geology, v. 28, p. 947–950.
- Wells, J.D. and Mullins T.E., 1973, Gold-bearing arsenian pyrite determined by microprobe analysis, Cortez and Carlin gold mines, Nevada: Economic Geology, v. 68, p. 187–201.
- Ye, Z., Kesler, S.E., Essene, E.J., Zohar, P.B., and Borhauer, J.L., 2002, Relation of Carlin-type gold mineralization of lithology, structure, and alteration: Screamer zone, Betze-Post deposit, Nevada: Mineralium Deposita, v.38, p. 22–38.